AI-directed voxel extraction and volume EM identify intrusions as sites of mitochondrial contact

Benjamin S. Padman,[1,3,5,*] Runa Lindblom,[1,2,4] and Michael Lazarou[1,2,3,4*]

[1]Aligning Science Across Parkinson's (ASAP) Collaborative Research Network, Chevy Chase, MD 20185, USA.
[2]Walter and Eliza Hall Institute of Medical Research, Parkville, Victoria, Australia
[3]Department of Biochemistry and Molecular Biology, Biomedicine Discovery Institute, Monash
[4]Department of Medical Biology, University of Melbourne, Melbourne, Victoria, Australia
University, Melbourne, Australia
[5]Present address: Telethon Kids Institute, Perth Children's Hospital, Nedlands, Western Australia, Australia

Correspondence: Benjamin S. Padman (benjamin.padman@uwa.edu.au), Michael Lazarou (lazarou.m@wehi.edu.au)

ABSTRACT

Membrane contact sites (MCS) establish organelle interactomes in cells to enable communication and exchange of materials. Volume electron microscopy (vEM) is ideally suited for MCS analyses, but semantic segmentation of large vEM datasets remains challenging. Recent adoption of artificial intelligence (AI) for segmentation has greatly enhanced our analysis capabilities. However, we show that organelle boundaries, which are important for defining MCS, are the least confident predictions made by AI. We outline a segmentation strategy termed AI-directed Voxel Extraction (AIVE), that combines AI predictions with image electron signals to confidently segment membrane boundaries irrespective of the AI model used. We demonstrate the precision conferred by AIVE by applying it to the quantitative analysis of organelle interactomes from multiple FIB-SEM datasets. Through AIVE, we discover a previously unknown category of mitochondrial contact that we term the mitochondrial intrusion. We hypothesise that intrusions serve as anchors that stabilize MCS and promote organelle communication.

Introduction

Organelles allow eukaryotic cells to compartmentalize cellular pathways that would normally be incompatible in a shared environment. However, compartmentalization also isolates key processes that depend on one another. To link isolated pathways, cells dynamically regulate interactions between organelles via physical points of contact called Membrane Contact Sites (MCSs) [1], that mediate inter-organelle communication, material exchange, tethering and structural support [2]. For example, cardiolipin synthesis at the inner mitochondrial membrane requires the precursor lipid phosphatidic acid, which is synthesised by the endoplasmic reticulum (ER) [3]; without adequate MCSs between mitochondria and the ER, cardiolipin synthesis would halt. MCSs are now widely accepted to be essential for cellular homeostasis [4], and MCSs have been reported between almost every conceivable combination of organelles [5-8]. Collectively, the interaction network between these various organelles is referred to as the "organelle interactome" [9].

Meaningful analysis of the organelle interactome poses a major technical challenge because MCSs represent small points of contact between comparatively large structures. Optical microscopy is suitable for imaging large interacting structures, but the separation distances of an MCS at 10 nm to 35 nm [10] are smaller than the resolvable limits of light. Biochemical methods also have limitations, since most sample preparation methods typically remove structural and spatial context from the MCS prior to analysis [11]. This is why volume electron microscopy (vEM) techniques are frequently referred to as the *"gold standard"* for studying MCS structure [10].

Volume EM (vEM) methods based on scanning electron microscopy (SEM), such as Focussed Ion Beam SEM (FIB-SEM) or Serial Block Face SEM (SBF-SEM), enable the ultrastructural visualisation of membrane structures within cellular scaled volumes. However, analysis of large vEM datasets poses a major challenge since the structures detected require semantic segmentation (hereafter segmentation) and object classification before they can be quantitatively analysed, and this process has historically relied on the manual labelling of each organelle membrane by hand to define their boundaries. This reliance on human input represents a major bottleneck in the throughput of vEM methods, and the traditional approaches to image segmentation can no longer keep pace with the rate of data acquisition [12], which increases every year [13]. Given these challenges, it can be argued that the rapid adoption of Machine Learning and Deep Learning based approaches for vEM was inevitable [14, 15]. AI-based image segmentation approaches are now widely accepted in the field of vEM, but they are not without their own potential flaws when it

comes organelle boundaries. Segmentation aims to define where an object is, but it also aims to define where an object isn't. The transition between the presence or absence of an object defines its bounding surface in a vEM dataset. The challenge arises when organelle surfaces segmented via AI-based approaches represent locations where a trained model was equally certain about the presence and absence of that object, and this can become problematic for MCS analyses.

Here, we demonstrate that the least certain model predictions made via AI-based image segmentation occur predominantly at the bounding surface of an object, which is the most important location for MCS analyses. This boundary uncertainty causes variable results between AI models, and directly impacts the reliability and accuracy of ultrastructural measurements. We outline and benchmark a strategy called AI-directed Voxel Extraction (AIVE) designed to negate this limitation. Through a series of benchmarking experiments, we demonstrate AIVE's capacity to reduce the variability between different AI models and confer greater consistency in MCS analyses in cultured cells and tissues alike. We conduct a comprehensive analysis of FIB-SEM datasets acquired from HeLa cells revealing the existence of a previously undescribed morphological category of mitochondrial MCSs that we term mitochondrial intrusions. The benefits of mitochondrial intrusions include increased surface area of membrane contacts between organelles that may serve as an anchor to enhance crosstalk efficiency.

Results

AI based approaches for the segmentation of volume EM data

AI based image segmentation uses information learned from training data to create statistical or deductive frameworks (termed a model), so that predictions can be made about new unseen data. Given the large datasets that can be generated using FIB-SEM imaging of cells, there are clear advantages in using AI based approaches to automate membrane segmentation [16]. To demonstrate, we used a test dataset of approximately 3.5 μm^3 in volume (Dimensions; X, 2.4 µm (740 px); Y, 1.2 µm (370 px); Z, 1.2 µm (121 slices)), that originates from a larger 655 μm^3 dataset that will be discussed later in greater detail (Fig.4-8). The test dataset was used to train a random forest model to identify cellular membranes detected via FIB-SEM imaging (Fig.1A-B). This trained model generated probability (P) values indicating the likelihood that a membrane is present at each voxel in the dataset (Fig.1C). To complete the segmentation of these membranes (Fig.1D-E), the scalar P values were binarized by assigning a probability threshold (Fig.1D) or an isosurface value (Fig.1E) to generate a 3D result. The decision threshold is a critical parameter in AI-based image segmentation, because it defines the boundary of each segmented object, thereby defining an object's volume, surface area and contact with other objects. When selecting a threshold value, a mid-point P value of 50% appears to be a logical choice (Fig D-E), but 50% probability values represent where the model was equally certain about the presence and absence of an object, making it the least certain prediction. Deep learning methods like convolutional neural networks (CNNs) do not use a pre-chosen decision threshold, but the output layer of a CNN learns parameters akin to a threshold in order to generate a binary result [17, 18]. Regardless of the methods used to predict and binarize results, the decision thresholds control the ultimate conclusions drawn by a model, and by extension, the boundary of each object.

When presented with the same data, different AI algorithms make different predictions about the boundaries of an object, and these differences can affect interpretations of organelle ultrastructure and membrane contacts [19]. To demonstrate this, we trained six machine learning models based on different algorithms of varying complexity to detect membranes in the same test dataset from Fig.1B. All six models were trained in the detection of membranes using the exact same training samples and feature data before application to the same test dataset (Fig.1F), and therefore any variability between results would be due to their algorithmic differences. Each model was capable of membrane detection (Fig.1F), but key differences existed between their

116 results. By visualizing the differences in predicted values (ΔV) from each model (Fig.1G; ΔV), it can
117 be demonstrated that most of the predictions agree between models, but the disagreements that
118 do occur are almost exclusively localized to the membrane boundaries (Fig.1G). This uncertainty
119 about the position of a membrane boundary would negatively impact the reliability of any
120 organelle contact analysis, since it confounds the measurement of membrane separation
121 distances.

122 AIVE: a tool for accurate automated segmentation of cellular membranes

123 To improve the accuracy of membrane boundaries obtained from AI segmentation methods, and
124 to generate greater consensus across different AI algorithms, we developed an approach termed
125 AI-directed voxel extraction (AIVE)[16, 20]. AIVE combines the automated segmentation outputs
126 of an AI model with the ground truth of the volume EM data. Applying AIVE involves two major
127 steps: 1) Segmentation of cellular membranes with an AI (as in Fig 1), and then 2) multiplication of
128 the AI membrane prediction with the original EM data to extract only those voxels belonging to a
129 membrane. The benefit of AIVE for membrane boundary detection is that the regions of uncertain
130 AI prediction are accounted for by the intensity of signals in the EM data. For example, at a
131 boundary where the AI is uncertain, if the EM voxels have little to no intensity then the AI
132 prediction of the uncertain region will not contribute to the output (Fig S1A).

133 To demonstrate the overall AIVE approach, the sample EM data and AI predictions from Fig 1 were
134 applied to the AIVE workflow. First, the AI prediction was smoothened by applying a 3D Gaussian
135 blur to reduce variability between predictions (Fig.S1C). The EM data was processed using
136 Contrast Limited Adaptive Histogram Equalisation (CLAHE) (Fig.2C) to normalise differences in
137 image contrast that can occur between different data acquisitions, and median blurred to reduce
138 signal shot noise. In the final step, the voxel values from the AI predictions and the raw EM data
139 (Fig.2B-C) were multiplied to generate the AIVE output (Fig.2D). By multiplying voxel values from
140 two independent dynamic ranges (Fig.S1A), any input voxels with a value of zero were
141 automatically excluded from the output, whereas electron signals predicted by the model to
142 represent membranes were retained for segmentation (Fig 2D and Fig S1A). Importantly, this
143 strategy is not limited to membranes, since any cellular content that generates an electron signal
144 can be isolated (Fig.S1B). Like any other segmentation technique, a threshold value is required to
145 generate 3D surfaces from the AIVE dataset (Fig.S2A-C). it is important to note that values near
146 the centre of the output dynamic range (50%; 8-bit value of 128) are not equivalent to the 50%

147 probability threshold value discussed earlier (Fig.1D). This is because AIVE results are the product
148 of multiplying two independent dynamic ranges (Fig.S1A), so the centre of both dynamic ranges is
149 in fact 25% (50% × 50% = 25%; 8-bit value of 64). The premise of AIVE is therefore akin to a signal
150 masking strategy, in which electron signals detected during EM are used for the segmentation of
151 object boundaries instead of using AI predictions alone (Fig.1G). Doing so improves the accuracy,
152 precision, and consistency of membrane segmentation, as we will demonstrate through a series of
153 benchmarking experiments.

154

155 Benchmarking AIVE

156 ***AIVE enables outputs to be compared between different AI algorithms***

157 We had observed large discrepancies between membrane boundary positions segmented by
158 different AI models in the same EM dataset (Fig.1F). To benchmark AIVE and demonstrate its
159 benefits, the same AI model predictions shown in Fig.1F were applied to the AIVE workflow
160 (Fig.2E). Upon application of AIVE, the difference in values (ΔV) between each model greatly
161 reduced (compare Fig.1F-G to Fig.2E-F). Quantitation of the ΔV per image slice also demonstrated
162 that the variability between results can be more than halved by AIVE, though we note that some
163 of this improvement was due to the initial blurring of the predictions (Fig.S1C). Next, we assessed
164 how the differences between boundaries from each model would affect 3D spatial measurements.
165 This was done by selecting 30 random points near membranes (distance probes; Fig.2H; see also
166 Video 1), then measuring the distance between each point and their nearest membrane (Fig.S2D).
167 By measuring the range (Fig.2I) and relative absolute deviation (Fig.2J) of distance values recorded
168 between models for each probe, the reliability of measurements under each condition can be
169 quantified. By both measures (Fig.2I-J), AIVE processing greatly improved the consistency of
170 measurements between models, outperforming the AI predictions alone with or without the
171 application of a Gaussian blur. Together, these analyses show that AIVE enables greater consensus
172 between AI models at regions of uncertainty (membrane boundaries), and that AIVE can be
173 applied with any AI model chosen by a user.

174 ***AIVE improves the accuracy and precision of organelle classification***

175 The accuracy of organelle membrane segmentation is fundamentally important for the analysis of
176 organelle interactions. The AIVE framework can easily integrate organelle classification prior to the

177 voxel extraction step. This simply requires the preparation of binary labels that map the identity of
178 organelles. For example, if a mitochondrion of interest were present in the dataset, its identity can
179 be defined by drawing a label around that approximate region (Fig.3A). While this process may
180 seem identical to conventional classification, AIVE differs in that it does not use these classification
181 labels to define the boundaries of any organelles. Instead, the class labels are used to mask
182 regions of the AI predictions and merely identify them as belonging to a specific organelle (Fig.3B-
183 C). The resulting data is then processed via AIVE resulting in segmentation of membranes
184 belonging to a specific organelle, which in the sample case is a mitochondrion (Fig.3D-E).

185 Class labels can be assigned manually by a human or automated using AI. To demonstrate this, we
186 assessed the classification labels generated by a human analyst and two U-Net CNNs in the
187 detection of one mitochondrion (Fig.3F) from the test dataset in Fig.1A. Classification by a human
188 analyst was conducted manually on two consecutive days, while the two U-nets differed in their
189 randomization seed during training. Mitochondrial labelling was generally similar between the
190 classification approaches (Fig.3F), but the human classifications tended to extend further than
191 necessary beyond the perimeter of mitochondria, whereas the U-Nets occasionally appeared to
192 miss portions of the mitochondrion (Fig.3F; arrowheads).

193 To benchmark the benefits of AIVE, the binary class labels from Fig 3F were used for organelle
194 segmentation using four different approaches: (1) Traditional instance segmentation, in which
195 binary class labels are used to define object boundaries (Fig.3G); (2) AI Extraction (AIE), where the
196 class labels are used to mask the AI predictions without voxel extraction (Fig.3H); (3) direct Voxel
197 Extraction (VE), which uses the class labels to mask the normalized EM data without using AI
198 predictions (Fig.3I); and, (4) AIVE (Fig.3J).

199 To understand the reconstruction results, we must first address the characteristics and limitations
200 of conventional 3D segmentation. Specifically, 3D surfaces generated using binary segmentation
201 alone (Fig.3G) demonstrate a noteworthy artifact called “terracing” (Fig.3G; see 3D insets), which
202 presents as artificial plateaus [21]. The terracing is caused by abrupt (binary) changes in voxel
203 value, which affect the local shape since contours can only be represented by a limited pool of
204 surface topologies (2^8; 256) [22], of which only 15 are unique [23]. In contrast, the additional
205 information present within a 8-bit scalar datasets, such as those generated by AIE, VE and AIVE
206 (Fig. 3H-J) can theoretically adopt $>1.8\times10^{19}$ (256^8) different polygon configurations at each voxel
207 and interpolate fractional angles with spatial anisotropy relative to the voxel grid [23]. Therefore,

208 by moving from binary labels to scalar values we can generate a more natural contour from our
209 voxel grid, as shown by the surface details shown in Fig. 3H-J compared to Fig. 3G.

210 Next, we benchmarked AIVE against voxel extraction (VE) and AI extraction (AIE). VE prevents
211 terracing (Fig. 3H), but the scalar data also includes irrelevant electron signals. Similarly, AIE
212 reduces terracing (AIE; Fig.4I), but the disadvantages of relying on AI predictions alone for
213 membrane boundaries have already been outlined (Fig.1-2). To directly show how the different
214 approaches influence the reliability of contact site analyses, we quantified the variability of
215 distance measurements between classification labels for each of the scalar 3D datasets (Fig.3H-J).
216 We conducted 3D measurements (Fig.3K) using a new set of 3D distance probes nearer to a
217 mitochondrion (Fig.S1D; see also Video 2), since the original 3D probe locations had no relation to
218 a specific organelle (Fig.2H). As demonstrated by the range (Fig.3L) and relative absolute deviation
219 (Fig.3M) of distance values recorded by each 3D probe, the distance measurements recorded for
220 AIVE datasets were very consistent between each of the differing class labels as opposed to VE
221 and AIE (Fig.3F). Therefore, AIVE substantially improves the precision and consistency of 3D spatial
222 measurements in volume EM datasets.

223 We next conducted a benchmarking experiment to compare the accuracy of measurements
224 generated via AIVE to a known standard point of reference. Nuclear Pore Complexes (NPCs) are
225 large protein channels in the nuclear envelope which mediate cargo transport between the
226 interior and exterior of the nucleus. NPC structure is highly conserved among eukaryotes, which is
227 why they are often used as a reference standard for benchmarking microscopy methods [24]. The
228 test dataset used in figures 1-3 originated from a larger cellular volume that also contained a
229 portion of nuclear envelope (Fig.4B). Using the manual classification strategy described in Fig. 3A-J,
230 we processed a portion of the nuclear envelope containing 18 individual nuclear pores (Fig.S1E),
231 via VE (Fig.3N), AIE (Fig.3O), or AIVE (Fig.3P). The same 18 pores were isolated from each
232 processed dataset and aligned using the exact same transforms (see methods for further detail;
233 Fig.S1F) to compare each processing method (Fig.3Q-T) against recent NPC structures [25, 26].
234 Data processed by VE alone (Fig.3N) rarely yielded a detectable pore because they were often
235 occluded by irrelevant electron signals (Fig.3Q). In contrast, central transport channels were
236 consistently detected in the data processed AIE alone (Fig.3O) or AIVE (Fig.3P), but the average
237 diameter of those pores differed between processing methods (Fig.3Q); 42.9 nm for AIE alone
238 compared to 52.4 nm for AIVE. We related these pore measurements to reported values from two

239 independent studies from 2021 (arrowheads in Fig.3Q), which used cryo-electron tomography to
240 resolve NPC structures *in cellulo* [25, 26]. Schuller *et al.* reported that human NPCs have a central
241 channel diameter of 57 nm (Fig.3Q; black arrowhead) [25]. The AIE processed data differs from
242 this value by 14.1 nm, whereas the AIVE results differed by only 4.6 nm. The study by Zimmerli *et*
243 *al.* was not conducted in human cells [26], but we include their findings because they provide
244 valuable context for the distribution of our measurements (Fig.3Q; value range indicated by white
245 arrowheads). Unlike data processed using VE or AIE alone, the majority of the AIVE processed
246 nuclear pores had a diameter within the published reported range. Renderings of the median
247 averaged pores from each processing method are also provided (Fig.3R-T; shown in purple), for
248 visual comparison with the human NPC structure published by Schuller *et al.* (Fig.3R-T; shown in
249 orange [25]). Collectively, our benchmark experiments show that AIVE processing substantially
250 improves both the precision and accuracy of spatial measurements in volume EM datasets.

251

252 Mapping organelle interactomes using AIVE

253 ***Compositional analysis of cellular membranes via AIVE***

254 Having outlined the technical basis and advantages of AIVE, we next demonstrated some of the
255 biological insights AIVE can yield when applied to large volume datasets. We aimed to characterise
256 mitochondrial interactions with other cellular organelles in three FIB-SEM datasets from HeLa cells
257 that were processed using AIVE (Set #1, Fig.4B; Set #2, Fig.4C; Set #3, Fig.4D; see Video 3). As
258 mentioned previously, the test dataset used in our benchmarking experiments (Fig.1-3) originated
259 from a small region (Fig.4A) within one of these datasets. AIVE data can be subjected to a wide
260 range of analyses (Fig.4-8), the simplest being direct quantification of membrane volume (Fig.4F-
261 H). Set #1 (654.0 μm^3 total volume of dataset) contained the highest proportion of organellar
262 membranes (84.7 μm^3; 12.9% of total volume). Due to the prominence of the cellular nucleus in
263 sets #2 & #3, organellar membranes represented a substantially lower proportion of their total
264 volume (Set #2, 858.8 μm^3 total, 59.4 μm^3 organellar membrane; Set #3, 640.9 μm^3 total, 39.1 μm^3
265 organellar membrane). The nucleus in Set #2 is noteworthy (Fig.4C), as it also contained multiple
266 examples of nucleoplasmic reticulum tubes spanning the interior of the nucleus [27]. Excluding the
267 nuclear envelope from subsequent analyses reveals striking similarities in the distribution of
268 membrane between organelles across the datasets (Fig.4E-G), with the ER being the most
269 abundant category of organellar membrane, followed closely by mitochondrial membranes.

270 Intracellular vesicles and Golgi apparatus were the next most abundant categories of organellar
271 membrane, but Golgi apparatus was not detected Set #2 (Fig.4F); coincidentally, Set #2 also
272 contained a lower proportion of early and late endosomal membranes than in the other two
273 datasets. To explore these datasets in greater detail, we next turned our attention to individual
274 mitochondria.

275 ***Quantitative analysis of mitochondrial morphology via AIVE.***

276 The three datasets (Fig.4B-D) collectively contained 186 individual mitochondria. Morphometric
277 analysis of these mitochondria based on their membranes alone would have limited value, since it
278 wouldn't include the mitochondrial interiors or bulk morphology, which is why our machine
279 learning models were also trained to classify materials other than membrane. For example, the
280 prediction results for "Matter" (Class 3), are specifically designed to represent any electron dense
281 non-membranous materials such as the mitochondrial matrix (Fig.S1B). This additional class
282 allowed us to "fill" the mitochondria by multiplying the matter class with the mitochondrial class
283 labels, then adding the result to the AIVE membrane outputs for the corresponding mitochondria.
284 In addition, the filling process enables imputation of the matrix of each mitochondrion.

285 Morphometric analyses, including measurements of mitochondrial volume, membrane surface
286 area, volume of matrix, shape, and length were applied to all 186 mitochondria. Based on the
287 morphometric analyses, six outlier mitochondrial morphologies were identified (Fig.5A-F). This
288 included the smallest mitochondrion, whose total volume was only 0.035 μm^3 (Fig.5A). As a point
289 of comparison, the smallest mitochondrion was approximately one-hundredth the volume of the
290 largest mitochondrion (Compare Fig.5A with Fig.5B), demonstrating a wide range of mitochondrial
291 size. Unsurprisingly, the largest mitochondrion also possessed the greatest membrane surface
292 area (25.079 μm^2), largest volume of membrane (1.863 μm^3), and largest volume of matrix (1.605
293 μm^3) of any detected mitochondrion (Video 4). Our analyses of mitochondrial morphologies also
294 included two different metrics of mitochondrial "length" (see Video 7), in which the most
295 elongated and longest mitochondria were identified. The most elongated mitochondrion (Fig.5D;
296 11.89 aspect ratio, 9.36 µm longest-optimal path) was identified by measuring mitochondrial
297 ellipsoid aspect ratios (major axis/minor axis; Fig.5J), whereas the longest mitochondrion (Fig.5E;
298 2.91 aspect ratio; 11.229 µm long) was determined by skeletonizing the bulk mitochondrial
299 structure, then measuring the longest-optimal path through the skeleton (Fig.5K). Mitochondrial
300 sphericity was also quantified (Fig.5L; Video 5, left), leading to the identification of the most

301 spherical mitochondrion (Fig.5F; sphericity = 0.860). The wealth of morphological data that was
302 obtained also allowed us to identify the most average mitochondrion (Fig.5G, and Video 5, right),
303 that had morphological measurements closest to the average value across every metric quantified.
304 Interestingly, we also noted that mitochondrial membrane volume correlated closely (R > 0.99)
305 with matrix volume in all datasets (Fig.5I), demonstrating that internal mitochondrial architecture
306 is tightly controlled despite large variations in morphology.

307 The morphometric analyses also led to the identification of mitochondrial nanotunnels based on
308 the separation of mitochondrial matrix volumes within a mitochondrion (Fig.5C; Video 5, center).
309 The presence of mitochondrial nanotunnels in HeLa cells was unexpected since nanotunnels are
310 typically observed in cellular/tissue environments in which mitochondrial movement is physically
311 constrained [28]. To show an example of nanotunnels in a physically constrained tissue, and
312 demonstrate AIVE's utility in tissue samples, we conducted FIB-SEM and AIVE of murine skeletal
313 muscle tissue (Fig.S3). Numerous examples of mitochondrial nanotunnels were observed (Fig.S3A-
314 C; Video 6), in which mitochondria remained interconnected over distance by reaching around
315 myofibrils via nanotunnels (Fig.S3, Video 6). In addition, we observed extensive sarcoplasmic
316 reticulum networks that contacted mitochondrial nanotunnels at sites around myofibrils.
317 Collectively, these analyses show the extensive mitochondrial morphology analyses that can be
318 conducted using AIVE, across cultured cells and tissue.

319

320 ***Quantitative analysis of the mitochondrial organelle interactome via AIVE.***
321 Next, we aimed to investigate the interactions between mitochondria and other organelles,
322 including MCS, by quantifying the separation distances of each mitochondrion from the ER, early
323 endosomes (EE), late endosomes (LE), lipid droplets (LDs) and general cytosolic vesicles (VE)
324 (Fig.6). By individually indexing each mitochondrion, we were also able to quantify the separation
325 between each mitochondrion and the remainder of the mitochondrial network.

326 First, we determined the closest approach made between organelles by measuring the minimum
327 separation distance for each mitochondrion relative to each category of organelle (Fig.6A-F).
328 Closest approach values for the EE, LE, and LD organelle categories varied greatly between
329 mitochondria (Fig.6C-E), which were often several microns away from these categories of
330 organelle (Fig.6C-E). Next, the number of mitochondria in contact with each category of organelle

331 was determined by applying the standard criteria often described for membrane contact sites of <
332 35 nm separation [10]. On average, we found that 12.13% of mitochondria were in contact with an
333 early endosome, 24.96% were in contact with a late endosome, and 10.24% were in contact with a
334 LD (Fig.6G). In contrast, every mitochondrion was found to be in contact with the ER (Fig.6G), and
335 the mitochondria-ER closest approach distances never exceeded 5nm (Fig.6B). These results are in
336 close agreement with the findings of Friedman et al., [29] who reported that all cellular
337 mitochondria maintain continuous contact with the ER. Additional categories of mitochondrial
338 membrane contact were also observed, and they included interactions with other mitochondria
339 and cytosolic vesicles (Fig.6G). These results demonstrate the utility of AIVE in measuring organelle
340 interactomes, while also revealing the extent of organelle contacts, and how they vary across
341 different organelles.

342

343 ***Mitochondrial intrusions are morphological platforms for organelle interaction.***
344 Using distance-based criteria to define MCS is a valuable tool. However, we also wanted to
345 account for the magnitude of the contact area relative to the size of an organelle because it gives
346 context to the breadth of a membrane contact site. For example, small point-like interactions with
347 randomly distributed vesicles (Fig.6G), cannot be distinguished from a membrane contact that
348 covers a substantially greater surface area. We therefore sought to refine our quantitative
349 analyses of MCS by accounting for the size of interaction sites between mitochondria with the ER,
350 vesicles (VE), and other mitochondria (Fig.6H-M). By grouping distance measurements into 5nm
351 brackets ranging between 0 to 250 nm, the percentage of a mitochondrion's surface from each
352 separation distance was determined (Fig.6K-M). The analysis revealed a prominent peak in the 0
353 to 5 nm distance bracket for mitochondrial (Fig.6K) and ER distance measurements (Fig.6L;
354 Arrowheads), but not for cytosolic vesicles (Fig.6M), that were typically further away from
355 mitochondria and occupied little of the mitochondrial surface.

356 The value peak detected in the 0-5nm range caught our attention because it is a large surface of
357 contact that cannot occur between round convex spheroids (Fig.S4A & C), unless one of those
358 objects partially envelopes the other (Fig.S4B & D). Indeed, our analysis of the 0-5nm membrane
359 contacts revealed striking mitochondrial morphologies that enabled membrane contact via
360 organelle intrusion (Fig.7). The intrusions were characterised by an invagination of the outer
361 mitochondrial membrane to form a narrow cavity that protruded into the interior of a

362 mitochondrion (Fig.7; see Videos 8-9). Mitochondrial intrusions frequently contained ER
363 membranes (Fig.7A-C; Video 8), that typically occupied the entire intrusion cavity. Interestingly,
364 the ER membranes often displayed higher levels of osmium staining (EM data; Fig.7A-C), indicating
365 that the membranes are protein rich or have a unique lipid profile. Mitochondrion-to-
366 mitochondrion intrusions were also observed, in which the exterior membranes of one
367 mitochondrion intruded into an adjacent mitochondrion (Fig.7D-E; Video 9). Unlike the ER-to-
368 mitochondrion intrusions, membranes in this category of intrusion did not display increased
369 osmium staining (Fig.7D-E). We also identified a mitochondrion that was intruding into another
370 mitochondrion while simultaneously receiving an intrusion from the ER (Fig.7D; Fig.8A, See box
371 indicating Set #1, mitochondria 61 & 89). This demonstrates that mitochondria can simultaneously
372 give and receive intrusions, potentially enabling inter-organelle communication. Mitochondrial
373 intrusions lacking an intruding membrane within the cavity were also observed (Fig.7F), indicating
374 that intrusion cavities may form independently from an intruding membrane.

375 We asked why mitochondrial intrusions have not previously been reported using established EM
376 approaches. Additional morphological analyses revealed key features that can provide an
377 explanation why intrusions have not been observed until now. Of the 186 mitochondria surveyed,
378 we detected a total of 50 mitochondrial intrusions among 36 individual mitochondria (Fig.8A),
379 equating to 0.269 intrusions per mitochondrion on average. No mitochondrial morphological traits
380 appeared to correlate with the presence of an intrusion (Fig.8B), implying that the formation of a
381 mitochondrial intrusion is stochastic. Indeed, the average number of intrusions per mitochondrion
382 (0.269) was used to model a Poisson distribution that closely approximates the observed values
383 (Fig.8C). Compared to the mitochondrion, the internal volume of the average intrusion cavity was
384 miniscule (Fig.8D), and the largest sphere capable of fitting within these cavities would have a
385 radius no larger than 50.6 nm (Fig.8E), yet they often extended several hundred nanometers
386 inward (Fig.8F).

387 A mitochondrial intrusion can only be confidently identified when viewed in its entirety. This is
388 because without evidence of the entrance, an intrusion would be indistinguishable from a
389 membrane inclusion (see Fig.7D), and without evidence of the deeper intrusion, the cavity
390 entrance would appear to be a slight membrane indentation (see Fig.7A). We sought to
391 demonstrate this by calculating the probability of detecting a fully intact mitochondrial intrusion
392 via TEM imaging by using Buffon's needle problem [30]. Buffon's needle problem is a geometrical

393 probability and is formulated as follows: If a needle of known length (L) is randomly dropped onto
394 an array of regularly spaced lines separated by a known distance (d), what is the probability that
395 the needle will overlap a line after landing (Fig.S4E). In the present context, the "needles"
396 represent mitochondrial intrusions with an average length (L) of 367.5 nm (Fig.8F), the space
397 between lines represent TEM sections of known thickness (d), and the needles that overlap a line
398 represent incomplete intrusions that extended into adjacent sections. The probability of detecting
399 a fully intact intrusion can therefore be considered the inverse of Buffon's needle problem (Fig.8G;
400 Fig.S4E). For a hypothetical 100nm TEM section (d = 100 nm) containing a mitochondrial intrusion,
401 there is less than a 1 in 10 chance (P = 0.087) that the intrusion will remain fully intact within that
402 section (solid line in Fig.8G). Under these conditions, an observer would be twice as likely to
403 observe only half of the intrusion (P = 0.177964; see dashed line, Fig.8G), which would be
404 indistinguishable from a membrane inclusion or indentation of the outer membrane. Even if the
405 section thickness was equal to the length of an intrusion (L = d), the probability of the structure
406 being intact remains low (P = 0.363; solid line in Fig.8G). It is important to note that the real
407 probability of observing an intrusion is likely even lower, since they were only present in a fraction
408 of the mitochondria (Fig.8C). In contrast, there would be a 95% chance (P = 0.953) of an intrusion
409 remaining intact if the Z-depth of the sampled volume spanned 5 µm (d = 5000 nm), which would
410 not be possible using TEM, but easily achieved via FIB-SEM. These calculations demonstrate why
411 mitochondrial intrusions have not previously been identified using historical TEM.

412 Taken together, by using AIVE we were enabled to discover that HeLa cell mitochondria can
413 contact the ER (and other mitochondria) via intrusion sites (Fig.7 & 8), which provide a larger
414 interface for surface interactions not possible between round objects (Fig.7; Fig.S4). We have also
415 shown that these intrusion sites are more likely to be indistinguishable from a mitochondrial
416 membrane inclusion when viewed by TEM (Fig.8G).

417

418 ## Discussion

419 In this study, we have outlined and benchmarked a technique termed AIVE for volumetric EM.
420 AIVE enables electron signals detected via FIB-SEM to be processed for rapid 3D reconstruction
421 and analysis with high fidelity. AIVE's fidelity is achieved by using the ground truth of EM data in
422 the final output. In AI research, ground truth is used to describe the preferred result from a

423 trained model [31], but the original definitions of ground truth specify that it originates from
424 objective empirical measurements [32]. In the context of this manuscript, the back-scattered
425 electron signals acquired via FIB-SEM imaging represented the most objective and empirical
426 measurements that could be used for ground truth. AIVE therefore uses an objective definition of
427 ground truth by linking AI predictions to real empirical measurements. Since its inception, AIVE has
428 been applied to volumetric EM analyses of cultured cells [16, 20] and animal tissues alike (Fig.S6).
429 However, in the absence of benchmarking, it was unclear why a cell biologist might choose to
430 apply AIVE versus AI predictions alone. Here, we demonstrate that membrane boundaries are the
431 least certain areas of AI predictions. Through extensive benchmarking, we make a case for the
432 benefits of AIVE to define membrane boundaries with high fidelity that provides benefits for the
433 study of organelle ultrastructure and MCSs.

434 Mitochondrial membrane ultrastructure is tightly linked to the biochemical functions of a
435 mitochondrion [33]. For example, mitochondrial damage and dysfunction are linked to a range of
436 abnormal mitochondrial morphologies including cristae disturbances and network fragmentation
437 [34-36]. In mitochondrial diseases, abnormal morphologies can manifest as osmiophilic inclusions
438 of concentric membranes and "onion-shaped" cristae within the mitochondria [34, 35], while in
439 other cases cristae structures are diminished [37]. Mitochondrial ultrastructure can also change in
440 response to the metabolic activity of mitochondria [38], in which mitochondria undertaking
441 oxidative reactions retain defined cristae whereas those enriched in reductive reactions lack
442 cristae. The intimate association between mitochondrial structure and function lends itself to
443 exploration using volumetric EM. AIVE can therefore be used in various contexts, ranging from
444 understanding mitochondrial ultrastructure in different tissues and disease states, to
445 understanding the relationship between mitochondrial morphology and physiological and
446 biochemical status. Cristae are intricate structures of the mitochondrial inner membrane that
447 come in all manner of unusual shapes and sizes depending on cell type and metabolic status [37].
448 For example, cristae in astrocytes appear to take the shape of triangles, whereas cristae in adrenal
449 cortex cells are highly circular [33]. Cristae analyses such as these have typically been conducted
450 using 2D TEM. By applying volume EM and AIVE, we anticipate that additional fascinating features
451 of cristae structure and biology will be revealed.

452 Mitochondrial structures can dynamically adapt according to their cytosolic environment. For
453 example, mitochondria in muscle tissue form nanotunnels that enable connectivity of the

454 mitochondrial network around the physical obstruction of myofibrils [28, 39](Fig. S6). Nanotunnel
455 connectivity can increase in murine cardiac myocytes with defective calcium release from the
456 sarcoplasmic reticulum [40], indicating an adaptive role for nanotunnels. Through AIVE, we were
457 able to expand on previous studies of nanotunnels and show the extensive ultrastructure of
458 mitochondrial nanotunnel networks in murine skeletal muscle (Fig. S6B). We also revealed
459 extensive MCSs between nanotunnels and the sarcoplasmic reticulum (Figure S6C), that may play
460 a role in calcium buffering during contraction [40]. Our findings demonstrate the benefits of
461 collecting large EM volumes combined with AIVE in identifying long distance organelle
462 connections, including mitochondria via nanotunnels, and the nucleus via nucleoplasmic tubes (Fig
463 4C).

464 Another area of cellular biology illuminated by AIVE and volume EM was the visualization and
465 quantitation of MCSs. Through AIVE, we were enabled to undertake high resolution analyses of
466 organelle interactomes via MCSs (Figs. 5-7). The value of AIVE for MCS analyses was best
467 demonstrated by the discovery of a hitherto unknown form of mitochondrial contact that we term
468 the mitochondrial intrusion (Fig. 7). Through intrusions, mitochondria were observed to contact
469 other mitochondria or the ER. Intrusion relays in which a mitochondrion simultaneously contacted
470 the ER and other mitochondria were also observed. These interactions go beyond the binary MCSs
471 that are typically described and highlights the complexity of organelle contacts that can be
472 revealed by volume EM and AIVE. Indeed, in a previous application of AIVE with volume EM,
473 wholesale organelle-ome changes were observed in response to perturbation of a single organelle
474 family [20]. We note that mitochondrial intrusions form basally, and they are distinct from
475 previously reported mitochondrial cavities [41]. Mitochondrial cavities, induced by fragmenting
476 mitochondria through depolarization, differ greatly from intrusions in size and morphology, and in
477 contact characteristics including the lack of intramitochondrial contacts [41].

478 What might be the benefits of mitochondrial intrusions as a form of MCS? One answer is increased
479 surface area for interaction. The exterior of a mitochondrion is typically round and convex [42, 43],
480 but this is the least efficient geometry for mediating surface-to-surface interactions [44] (Fig.S3A).
481 Mitochondrial intrusions can maximize the surface area of an MCS (Fig.S3B), and therefore
482 promote the efficiency of inter-organelle communication [45]. Another potentially important
483 benefit of intrusions is that the increased contact area can serve as an anchor to stabilise an
484 otherwise fleeting MCS. Once formed, the very close proximity of membranes within intrusions (0-

485 5nm) can feasibly support tethers that support lipid transfer including the mitochondrial proteins
486 PTPIP51 and MIGA2 [46-48], that could be facilitated by Mfn1/2 for intramitochondrial intrusions,
487 and Mfn2 and VAPB for ER-mitochondria intrusions [49-51]. In contrast, MCSs involving IP3Rs
488 (inositol 1,4,5-triphosphate receptors) that facilitate calcium transfer between ER and
489 mitochondria might be too bulky for the very close contacts made by intrusions [1, 52].

490

491 Overall, we demonstrate the utility of AIVE combined with volumetric EM for understanding the
492 ultrastructure and interactome of cellular organelles, while also demonstrating its capacity to
493 reveal fascinating and unexpected features of cell biology, including the identification of
494 mitochondrial intrusions as a form of MCS.

495

496

497 **Acknowledgements:**

498 We acknowledge Gediminas Gervinskas and the Ramaciotti Centre for Cryo-Electron Microscopy,
499 Monash University for technical support with electron microscopy. And we thank Matthew Eramo
500 and Mike Ryan for the mouse tissue FIB-SEM dataset, and acknowledge Monash Animal Research
501 Platform, Monash University. The study is funded by the joint efforts of The Michael J. Fox
502 Foundation for Parkinson's Research (MJFF) and the Aligning Science Across Parkinson's (ASAP)
503 initiative. MJFF administers the grant ASAP-000350 (to ML) on behalf of ASAP and itself.

504

505 **Methods**

506 **Cell culture**

507 HeLa cells were cultured Dulbecco's modified eagle medium (DMEM) supplemented with 10 %
508 (v/v) FBS (Cell Sera Australia), 1 % Penicillin-Streptomycin, 25 mM HEPES, 1x GlutaMAX (Life
509 Technologies) and 1x non-essential amino acids (Life Technologies). Samples were prepared by
510 culturing HeLa cell monolayers on a polymer film substrate (Aclar film; 203.2 µm thick;
511 ProSciTech), which was heat-welded to the plastic surface of a 10 cm tissue culture dish with a
512 soldering iron. Three dishes were prepared, and UV sterilized before seeding approximately 6 x

513 10^6 HeLa cells onto the Aclar film in each dish. The cells were allowed to attach under normal
514 culture conditions for 48 hrs, with replacement of the culture medium 1 hr prior to fixation.

515 Sample preparation of HeLa cells for FIB-SEM

516 The samples were chemically fixed with 4 % paraformaldehyde in 0.1 M phosphate buffer (pH 7.2)
517 at 37 °C for 1 hour, with overnight postfixation with 2.5 % glutaraldehyde in 0.1 M sodium
518 cacodylate buffer at 4 °C. Each polymer film was detached from their tissue culture dish before
519 being transferred to a polypropylene tray (lid of a pipette tip box) where they were immobilized by
520 heat-welding with a soldering iron. A BioWave Pro microwave system (Pelco) was used for
521 microwave assisted sample processing in all subsequent stages. Osmication was conducted using a
522 modified OTO method [53] with three microwave duty-cycles (120 s on, 120 s off) at 100 W under
523 vacuum where indicated in the following stages; 2 % (w/v) OsO_4, 1.5 % (w/v) $K_3Fe(CN)_6$ in 0.1 M
524 cacodylate buffer (pH 7.4) at 4° for 2 hours, followed by microwave processing; three MilliQ water
525 rinses; 1 % (w/v) Thiocarbohydrazide in water with microwave processing; three MilliQ water
526 rinses; then, 2 % OsO_4 in water with microwave processing. After further MilliQ water rinses, the
527 samples were *en bloc* stained with 2 % (w/v) aqueous uranyl acetate [54], followed by Walton's
528 Lead Aspartate [55], with each stain requiring three microwave duty-cycles (120 s on, 120 s off) at
529 100 W under vacuum. Microwave assisted dehydration (150 W for 40 s per stage) was performed
530 by graduated ethanol series (80 %, 90 %, 95 %, 100 %, 100 % (w/v)) followed by propylene oxide
531 (100 %, 100 % (w/v)). The samples were infiltrated with a modified Araldite 502/Embed 812 resin
532 of the following composition (described for 10 ml resin); 2.20 g Araldite 502, 3.10 g Embed 812,
533 3.05 g NMA (nadic methyl anhydride), 3.05g DDSA (dodecenylsuccinic anhydride), and 400 µL
534 BDMA (benzyldimethylamine). Infiltration was conducted using a graduated concentration series
535 in propylene oxide (25 %, 50 %, 75 %, 100 %, 100 % (v/v); 180 s at 250 W under vacuum). Final
536 embedding was conducted with minimal resin, which was polymerized at 60 °C for 48 hrs.

537 The Aclar film was peeled from each of the resin embedded cell monolayers, before using a
538 hammer to sub-divide the resin into a random assortment of shards that were pooled into a single
539 collection. Sample shards were blindly taken from the sample pool, deposited on a small droplet
540 of the Araldite 502/Embed 812 resin on the tip of a 3.2 mm diameter aluminium rod; another
541 droplet of resin was then placed on top of that shard so that another randomly selected shard
542 could be placed on top, and the process was repeated to embed sandwiches of randomly oriented
543 cells at least three monolayers thick, before final polymerization at 60 °C for 24 hr. The stacked cell

544 monolayers were hand trimmed with a razor blade before trimming with a glass knife, to expose
545 multiple monolayers for 3D FIB-SEM imaging.

546 Data acquisition and pre-processing

547 FIB-SEM imaging was conducted three separate times on randomly selected cells, one cell was
548 chosen from each cell monolayer. Imaging was conducted using a cryo-Helios G4 UX FIB-SEM (FEI)
549 at room temperature using the TLD detector in immersion lensing mode for back-scatter electron
550 imaging at 3.255 nm per pixel (2 kV, 100 pA, 3 µs dwell time). Ion milling was conducted at 10 nm
551 per slice (Gallium, 30 kV, 9 nA) using the Auto Slice and View (v4.1; FEI) software. All datasets were
552 spatially registered (rigid transform) using the virtual stack registration plugin in FIJI (v1.53t) [56,
553 57]. The signal normalized inputs for AIVE were generated using a pseudo-3D implementation of
554 contrast limited adaptive histogram equalisation (CLAHE), in which three different 2D CLAHE
555 calculations were made from the front (XY), top (XZ), and side (YZ) of the registered dataset. Each
556 2D calculation was made using a modified version of the CLAHE plugin released by Stephan
557 Saalfeld in 2009; this modified plugin accounts for the anisotropy of voxels in the XZ and YZ
558 directions by allowing the use of rectangular sliding window during CLAHE. The modified plugin
559 ("CLAHE_Anisotropic.class") and script for batch automation
560 ("Batch_3DCLAHE_AnisotropicXYZ.ijm") are both provided on GitHub
561 (https://github.com/BenPadman/AIVE.git).

562 Sample preparation & AIVE of mouse muscle tissue

563 Wildtype C57BL/6J mouse was anaesthetised at 3 weeks of age prior to dissection of the tibialis
564 anterior muscle, which was immersion fixed in 4% PFA in 0.1M phosphate buffer at room
565 temperature (1 hour). Tissue was further dissected under fixative to extract 1mm cubed samples,
566 which were immersed in secondary fixative (4% PFA, 2.5% GA in 0.1M phosphate buffer) for
567 24hrs. All subsequent sample processing stages and imaging conditions were conducted as
568 described above for cultured cell samples. Two separate FIB-SEM datasets of skeletal muscle were
569 acquired. A machine learning model was trained on 3 classes of voxel designated "Cytosol",
570 "Fibrils" and "Membrane", using 120,000 samples per class (360,000 total) to train the final model
571 with a 10-fold test cross-validation result of over 97% self-accuracy. Mitochondria were manually
572 classified in MIB as described above, and all remaining membranes were designated as
573 sarcoplasmic reticulum. The final AIVE results were calculated as described above, and
574 reconstructed in 3D by marching cubes with an isovalue of 64. All animal work was approved by

575 the Monash Animal Research Platform Ethics Committee (MARP #17628), Monash University,
576 Australia, and conducted in compliance with the specified ethics regulations.

577 Computational hardware

578 All presented analyses were conducted on one computer equipped with consumer-grade
579 hardware, which included an Intel® Core™ i9-9900KF CPU clocked at 3.60GHz (16 cores), 64Gb of
580 RAM at 2133MHz, one 2 Tb SSD (Samsung 970 EVO Plus) for short term storage during machine
581 learning feature calculation, two 8Tb HDD's in RAID1 for long-term storage of machine learning
582 features and results, and an Nvidia GeForce RTX 3080 Ti for deep learning and 3D rendering.

583 Machine learning

584 Machine learning was conducted within the Waikato Environment for Knowledge Analysis (WEKA
585 v3.9)[58]. Training features were extracted from the registered image data using the 3D Trainable
586 Weka Segmentation (TWS) plugin for ImageJ [59, 60]. As proposed in the original manuscript [59],
587 we wrote a series of custom scripts for the TWS plugin to expand and automate its capabilities;
588 these scripts have been provided on GitHub (https://github.com/BenPadman/AIVE.git). The scripts
589 were designed to minimize RAM storage requirements for general machine learning, by ensuring
590 that all image features required for training and evaluation are only calculated once prior to local
591 storage on a hard disk. Instead of calculating all features for the entire stack simultaneously, the
592 scripts only inspect a portion of the stack at a time while including the minimum number of
593 flanking slices required by the radius of a 3D image filter. This enables features to be calculated for
594 image stacks of arbitrary length at the cost of wasted computation on flanking slices. Furthermore,
595 the script generates features incrementally by grouping image filter calculations into subsets,
596 temporarily storing the results on a local hard disk, then merging them to generate final feature
597 stacks for each slice (see script: "PART1_3DFeatSplitter_Sigma8.bsh"). Our approach also includes
598 the calculation of additional custom 2D features (see script: "PART2_2DFeatSplitter.bsh"), which
599 are merged with the original 3D feature stacks (see script:
600 "PART3_Combine3Dand2DFeatures.bsh") allowing us to calculate 175 features per slice. The
601 scripts required to execute this process are provided. In a departure from the TWS plugin all
602 training annotations were generated externally, by using the Microscopy Image Browser (MIB) to
603 generate label images where each training class is defined by the numerical value of a voxel (value
604 of 1 for class 1, value of 2 for class 2, etc). A script was then used to import each training label
605 image into TWS with its corresponding feature stack (Fig. 1G), to extract feature measurements

606 from a predetermined number of randomly selected voxels per class (see script:
607 "CorePartA_ExtractTrainingData_ArbitraryClassNum.bsh"). The feature data extracted via this
608 script can then be pooled using the "append" function in WEKA, then imported into WEKA Explore
609 for analysis and machine learning to generate various trained models, as was shown in Figures 1-3.
610 These trained models are loaded by a final script
611 ("CorePartB_ApplyClassifierToFeatureStacks.bsh"), which is designed to evaluate pre-existing
612 feature stacks.

613 These scripts were used for machine learning throughout the manuscript as follows. The analyses
614 in figures 1-3 used models trained to detect three classes of material; "Sol" (Class 1), representing
615 granular protein content of the cytoplasm and nucleus; "Matter" (Class 2), representing electron-
616 dense homogenous materials that do not belong to a membrane (i.e. mitochondrial matrix);
617 "Memb" (Class 3), representing genuine cellular membranes. The division of non-membranous
618 materials into two classes was aimed to account for the class imbalance problem; Training
619 annotations were drawn by hand in MIB. For the analyses shown in figures 1-2, feature stacks for
620 each of the three altered test datasets were generated separately before using a shared pool of
621 training labels to extract feature measurements for 1500 voxels per-class-per-slice from eight
622 slices (12000 samples per class, 36000 samples per stack, 108000 feature measurements total).
623 For the training of the six models in Figures 1-2; RF (Random Forest), J48 (the java compatible
624 extension of Ross Quinlan's C4.5 classifier), MLP (Multi-Layer Perceptron), DT (Decision Table),
625 JRip (java compatible propositional rule-based RIPPER), and PART (Projective Adaptive Resonance
626 Theory neural network), algorithm specific parameters are enclosed within the training logs we
627 have provided for each model (See GitHub: https://github.com/BenPadman/AIVE.git). Differences
628 between model outputs were calculated using ImageJ, by calculating the absolute difference in
629 predicted values (ΔV) at each voxel between each model and every other model; results were
630 visualized by averaging all ΔV comparisons for a given model when compared to all others.

631 Data shown in Figures 4-8 used pooled feature data from all three datasets to train a random
632 forest classifier as described above, except that training involved five unique classes of material.
633 The first three of these classes were used to detect non-membrane materials: "Void" (Class 1),
634 representing the homogenous extracellular regions that lack an electron signal; "Sol" (Class 2),
635 representing granular protein content of the cell and nucleus; "Matter" (Class 3), representing
636 electron-dense homogenous materials that do not belong to a membrane (i.e. mitochondrial

matrix). The remaining two classes (4 & 5) were sub-categories of membrane: “Memb” (Class 4), representing the majority of cellular membranes, and “Vesc” (Class 5) to represent vesicular membranes; the membrane sub-classes needed to be merged together to generate a final AIVE result, but separation into two classes allowed the classification of cellular vesicles by machine learning alone.

Organelle classification for AIVE

Some of the raw classifier outputs described above were exploited to assist the classification of organelles. For example, dilation of the “Void” class was used to assist classification of the plasma membrane, whereas the Sol class labels in the nucleus were used to assist annotation of the nuclear envelope. Manual labelling in MIB was then used to classify the Golgi apparatus, early endosomes, late endosomes, lipid droplets. The mitochondria were also classified in this way, but multiple sub-classes were used to ensure that adjacent un-fused mitochondria were considered independently from one another, thus allowing each individual mitochondrion to be indexed for independent analyses. The ER was classified through a process of elimination; it was the only remaining unclassified membrane after classification of all other organelles. Final class labels were exported from MIB as a label image. The label images containing all class labels were separated into individual binary stacks, with each image representing one class of organelle. These binary stacks were blurred with a 10nm gaussian filter. The 32-bit predictions generated for “Memb” and “Vesc” (Classes 4 &5; described above) were combined, then multiplied with the binary stacks and blurred with a 10nm gaussian filter, before merging the results with 3D CLAHE results calculated earlier. This generates the final AIVE results for each individual organelle class.

U-Net training

Two U-Nets with 3D anisotropic architecture (same padding) were trained via stochastic gradient descent with momentum (SGDM; 0.001 weight decay; 0.9 momentum), using 80×80×80 voxel input patches (1040 x 1040 x 1600nm in XYZ), 5×5×5 filters, leaky ReLu activation layers (0.001 scale), and a dice pixel classification layer. Both U-Nets were structured with 16 input filters and 4

666 layers, and data augmentations (both 2D & 3D) were applied to 80% of the input patches during
667 training with a piecewise learning schedule (initial learn rate of 0.01; dropping by 80% every 5
668 epochs) for 35 epochs (512 iterations per epoch). The only difference between these two U-Nets
669 was the random seed value used during network initialization; The first U-Net used a random seed
670 of 1337, while the second used a value of 1338 (Fig.3F). To minimize segmentation discontinuities
671 between adjacent prediction tiles [61], each U-Net was applied using 5% tile overlap with four
672 different orientations of the dataset (original, X-flipped, Y-flipped, Z-flipped). The results were
673 then returned to their original orientations before averaging to create an ensemble result. Image
674 classification by a human image analyst in the same figure was conducted on two consecutive days
675 and required approximately 10 minutes to complete.

676

677 **3D Distance Probes**

678 To simulate the effect of result variation on membrane contact site measurements, all static
679 distance probes were assigned in accordance with standard criteria for designation of a contact
680 site (< 35 nm separation; [10]). Initial coordinates for the 3D distance probes were chosen by
681 running a stochastic simulation of diffusion limited aggregation in Mathematica (version 9). These
682 coordinates were annotated in a blank TIFF stack with identical dimensions to the test dataset, by
683 converting the voxel located at each indicated coordinate from black (value of 0) to white (value of
684 255). Probe coordinates further than 35nm from (or inside) a membrane were removed from the
685 collection by binarizing the membranes shown in Fig. 1C, dilating them by 35 nm, then subtracting
686 the un-dilated membranes from the result; any 3D probes outside the boundaries of this result
687 were deleted. This process was repeated until 30 unique probe locations were identified (Fig.2H).

688 Analyses of mitochondrial membranes (Fig.3G-M) required an additional set of criteria for the
689 distance probes, since the original 3D probes were generated without relevance to any specific
690 organelle (Fig.1H) and most were located further than 35 nm from a mitochondrion. 3D probe
691 coordinates for mitochondrial membranes were therefore generated by using the same 35nm
692 membrane boundary mask described for general membranes above in combination with an
693 additional mask representing the mitochondria, as follows; All mitochondrial class labels shown in
694 Fig.3F were averaged, binarized, dilated by 35 nm, then applied in a boolean AND operation with
695 the 35 nm membrane mask used to define the first probe positions (Fig.1H). The resulting mask

696 was then used to assign new random points as described above, until thirty new random points
697 were defined within 35nm of a membrane and within 35 nm of the mitochondrial class label
698 (Fig.4K). Value range for distance measurements (Fig.2I; Fig.3L) were calculated by subtracting the
699 minimum recorded distance from the maximum recorded distance for one probe. Relative
700 absolute deviations (aka. relative mean absolute difference) in measurements from each probe
701 (Fig.2J; Fig.3M) were calculated by dividing the mean absolute difference (difference between
702 each measurement and the mean value) of measurements by the arithmetic mean of all
703 measurements from that probe, then averaging the result.

704 Nuclear pore analyses

705 Nuclear pores were initially chosen by defining the approximate 3D coordinates of each pore in
706 the raw dataset. A cuboidal region surrounding each coordinate (300 nm on each axis) was then
707 extracted from the raw (Fig.S1F), VE (Fig.3N), AIE (Fig.3O), and AIVE (Fig.3P) image stacks. These
708 pores were then arranged into an identical orientation as follows; All four representations of data
709 (raw, VE, AIE, & AIVE) for each pore were averaged to create datasets for inter-pore alignment,
710 without biasing toward any particular method. Using the Fijiyama plugin (V4.0.11) for FIJI (v1.53),
711 Each averaged pore was manually aligned to the next pore in the sequence to generate a
712 preliminary alignment between all 18 pores, which was then refined via automatic block-
713 matching, also through Fijiyama [62]. Individual transform operations describing this alignment
714 were then composed into one rigid transformation per nuclear pore, allowing each pore to be
715 aligned into the same orientation across all four processing methods. Feret diameters of the pores
716 were measured binarizing the pore, then applying the built-in “analyse particles” function in FIJI
717 (v1.53) at the centrally aligned slice of the pore. All depictions of the individual nuclear pores are
718 shown post-alignment (Fig.3N-P; Fig.S1F), to account for the variable orientation of some pores in
719 the original dataset (Fig.S1E).

720

721 3D rendering and numerical analyses

722 All 3D surfaces were generated using the marching cubes algorithm with octree binning (256
723 points per leaf) in ParaView (v5.7). Distance measurements and mapping for visualization were
724 conducted in ParaView, by calculating the signed distance field for one polygonal mesh then
725 measuring the field value at each vertex of a second polygonal mesh. The signed distance fields

were calculated using a custom ParaView filter proposed in a blog post by Cory Quammen (Technical leader in Scientific Computing Team; Kitware); the filter has been provided. All 3D renderings were generated using the Cycles render engine in Blender (v2.93). All other morphometric analyses were conducted using the MorpholibJ plugin for FIJI [63]. Difference in voxel values (ΔV) were calculated using the built-in “image calculator” function in FIJI (v1.53). Mathematica (version 9) was used for all other statistical analyses and charts, including the Buffon’s needle simulation in Fig.8.

Figure Legends:

Figure 1: Variable AI predictions predominantly occur at object boundaries during segmentation.

(A-E) 3D test data acquired via FIB-SEM imaging, showing an **(A)** overview and **(B)** inset 2D slice from dataset with **(C)** corresponding predictions generated by a random forest classifier trained to detect membranes, alongside **(D)** 2D binary segmentation and **(E)** 3D surfaces based on the membrane predictions. **(F)** 2D slices depicting raw membrane predictions for test dataset (from Fig.1B) with values (V) shown as percentage of their total dynamic range (0 to 1), made using six different machine learning algorithms (also provided as 3D renders in **Fig.S2A)**; RF (Random Forest), J48, MLP (Multi-Layer Perceptron), DT (Decision Table), JRip, and PART (Projective Adaptive Resonance Theory). **(G)** Visual depiction of the absolute difference in voxel values (ΔV) between each prediction from F, showing the average value difference for each 2-way value comparison as a percentage of the total dynamic range (0 to 1).

Figure 2: AI-directed voxel extraction (AIVE) minimizes the influence of variable AI predictions.

(A-D) Flow chart depicting the technical basis of AI-directed voxel extraction (AIVE), in which **(A)** raw 3D data from the FIB-SEM is used to **(B)** train and apply a classifier model to generate probability maps depicting the location of cellular membranes (dynamic range, 0 to 1), while **(C)** intensity values from the original dataset are normalized via CLAHE (dynamic range, 0 to 255); **(D)** values from B are then multiplied by values from C (see also **Fig.S1A**), which isolates the voxel values belonging to a membrane to generate raw AIVE data (application of AIVE to other classes of signal provided in **Fig.S1B**). **(E)** 2D slices depicting raw AIVE data generated using each algorithm shown in Fig.1F (3D renders of the same data provided in **Fig.S2C**), and **(F)** averaged ΔV values for each 2-way comparison between one AIVE output and each of the other outputs (both shown as a percentage of 8-bit dynamic range; 0 to 255). **(G)** Quantification of the average ΔV per slice for each 2-way comparison made between the model predictions (Fig.1F-G) and between AIVE outputs (E-F) generated using those same model predictions (quantitation and 3D renders of blurred AI predictions shown in **Fig.S1C** & **Fig.S2B** respectively). **(H)** 3D rendering of membrane surfaces from the test dataset (from Fig.1E) viewed from the front and above, indicating the

768 positions of the static 3D probes used to benchmark membrane distance measurements
769 (membranes nearest to each 3D probe are indicated by red shading; see Video 1 for rotation
770 animation depicting probe positions). **(I)** Quantification of the distance between each 3D probe
771 (shown in H) and the nearest membranes detected by the six models shown in Fig.1F (raw
772 distance measurements provided in **Fig.S2A**), after segmentation of the raw predictions, blurred AI
773 predictions, or AIVE outputs, showing **(I)** the range (min-max) for values reported by each probe
774 between models, and **(J)** the relative absolute deviation in measurements from each probe. Plot
775 markers in I-J indicate value for individual 3D probes. Interquartile range indicated by box, median
776 indicated by horizontal lines, minimum and maximum indicated by whiskers in G, I & J.

777

778 **Figure 3: Object classification does not alter the precision or accuracy of**
779 **segmentation by AIVE.**

780 **(A-E)** Flow chart depicting object classification during AIVE, in which **(A)** organelle labels and **(B)**
781 membrane predictions are multiplied to generate **(C)** a contextually masked membrane prediction,
782 **(D)** which is then combined with the normalized EM data to generate **(E)** AIVE data belonging to a
783 specific organelle. **(F)** 2D examples of mitochondrial classification labels provided by one human
784 on different days, or two 3D U-Nets with different initialization seeds. **(G-J)** 3D rendered results
785 classified using the labels shown in Fig.3F, after classification via **(G)** conventional instance
786 segmentation, or by using the binary labels **(H)** for selective voxel extraction (VE), **(I)** AI extraction
787 (AIE), or **(J)** AIVE. **(K-M)** Quantitative analysis of **(K)** the distance between mitochondrial
788 membranes and each mitochondrial 3D probe (probe locations shown in **Fig.S1D**; also see Video 2
789 for rotation animation depicting probe positions), **(L)** the range of values recorded by each 3D
790 probe, and **(M)** the relative absolute deviation in 3D probe measurements, for all datasets shown
791 in Fig.3H-J. **(N-P)** 2D maximum intensity projections of 18 individual nuclear pores, which were
792 spatially aligned prior processing and segmentation via **(N)** VE, **(O)** AIE, or **(P)** AIVE (Unprocessed
793 pores shown and pore locations shown in **Fig.S1E & F** respectively). **(Q)** Feret's diameter
794 measurements of the central transport channel from each nuclear pore after segmentation via VE,
795 AI or AIVE. (black arrowhead indicates diameter reported by Schuller *et al.* [25]; hollow arrowhead
796 range indicates diameters reported by Zimmerli *et al.* [26] indicated by). **(R-T)** 2D projections and
797 3D renderings showing the median averaged data generated via by **(Q)** VE, **(R)** AI, or **(S)** AIVE
798 (purple), with spatial alignment to the nuclear pore complex structure (orange) published in 2021

799 by Schuller *et al.* [25]. Plot markers in **K-L** indicate values for individual 3D probes. Plot markers in
800 **T** indicate measurement for individual nuclear pores. Interquartile range indicated by box, median
801 indicated by horizontal lines, minimum and maximum indicated by whiskers. Scalebars; **N-S**,
802 100nm.

803

804 **Figure 4: The compositional analysis of membranes in bulk cellular volumes via**
805 **AIVE.**

806 **(A-D)** 3D renderings of the three FIB-SEM datasets processed via AIVE for quantitative analysis,
807 showing **(A)** the test data used in Fig.1-3 alongside overviews of **(B)** the dataset it originated from
808 (Set #1; leading lines indicate location), and **(C-D)** two additional datasets processed via AIVE (Set
809 #2 & Set #3 respectively). All three overviews are shown at the same scale (See Video 3 for
810 animated cutaways of the data). **(F-H)** Compositional analysis of membrane volumes belonging to
811 non-nuclear cytoplasmic organelles in **(F)** Set #1, **(G)** Set #2, and **(G)** Set #3. See Video 3 for
812 animated cutaways of overview data. Scalebars; A, bounding box is 2400nm wide; B-D, markers on
813 scale grid for overviews are 1000nm apart.

814

815 **Figure 5: The morphometric analysis of individual mitochondria via AIVE.**

816 **(A-G)** Mitochondria of interest that were detected in the AIVE-processed datasets shown in Fig.4,
817 showing the membranes of each mitochondrion (Red) alongside its matrix (Blue), and the binary
818 skeleton calculated for its bulk morphology (Black; longest-optimal path endings shown in yellow);
819 these include **(A)** the smallest mitochondrion, **(B)** the largest mitochondrion, **(C)** a nanotunnelling
820 mitochondrion, **(D)** the most elongated mitochondrion, **(E)** the mitochondrion with the longest
821 continuous tubule, **(F)** the most spherical mitochondrion, and **(G)** the mitochondrion closest to the
822 average values detected by all morphological metrics. For animations of these data, see Video 4
823 (for **A & B**), Video 5 (for **C, F & G**), and Video 7 (for **D & E**). **(H-L)** Quantitative analysis of key
824 morphological metrics all mitochondria in each set; **(H)** box whisker chart for the total volume of
825 each mitochondrion, **(I)** a scatter chart of showing the relationship between the volume
826 membrane (x-axis) and volume of matrix (y-axis) in each mitochondrion, with **(J-L)** box whisker
827 charts showing additional metrics for **(J)** mitochondrial sphericity, **(K)** mitochondrial length, and **(L)**
828 mitochondrial elongation. See Video 4 Plot markers indicate value for individual mitochondria.

829 Hollow plot markers indicate mitochondria that were intersected by the dataset boundary; these
830 mitochondria were excluded from analyses sensitive to incomplete mitochondria (Fig.5 A, E, D, G,
831 J-L). Interquartile range for mitochondrial population indicated by box, median indicated by
832 horizontal lines, minimum and maximum indicated by whiskers. Scalebars; A-G, markers on scale
833 grid are 1000nm apart.

834

835 **Figure 6: AIVE for the analysis of the mitochondrial interactome.**

836 **(A-F)** Quantification of the closest approach distance separating each individual mitochondrion
837 from **(A)** the rest of the mitochondrial network, **(B)** the ER, **(C)** early endosomes, **(D)** late
838 endosomes, **(E)** lipid droplets, or **(F)** cytosolic vesicles. **(G)** Average percentage of all mitochondria
839 detected within 35nm of indicated organelle per set. **(H-J)** 3D rendering of distance-mapped
840 mitochondrial surfaces from a sub-region in Set #1. The mitochondrial surfaces are shaded with a
841 colorimetric scale indicating surface distances from **(H)** other mitochondria, **(I)** the ER, or **(J)**
842 cytosolic vesicles. **(K-M)** Surface area histograms for the mitochondria located within 100nm of
843 indicated organelle, depicting the average percentage of a mitochondrial surface located within
844 indicated distance of **(K)** other mitochondria, **(L)** the ER, or **(M)** cytosolic vesicles (Arrowheads in K
845 & L indicate the anomalous peak, explained in **Fig.S4A-D**). Plot markers in A-F indicate value for
846 individual mitochondria. Interquartile range indicated by box, median indicated by horizontal lines,
847 minimum and maximum indicated by whiskers. Data in G are mean ± S.D calculated for the
848 averages in each dataset. Histogram data in K-L are mean surface area percentages binned into
849 5nm distance brackets relative to the target organelle; mean values for each set are also shown.

850

851 **Figure 7: Mitochondrial intrusion sites facilitate membrane contact with the ER**
852 **and other mitochondria.**

853 **(A-C)** Examples of ER-to-Mitochondrion intrusion sites detected in **(A)** Set #1, **(B)** Set #2, and **(C)**
854 Set #3, displayed as partial (50nm) 2D averaged projections of raw EM and AIVE data (left panels),
855 rendered in 3D (centre panels), and with a colorimetric distance-map relative to the ER (right
856 panels). For animations of these data, see Video 8. Additional examples are provided in Fig.S5A-C.
857 **(D-E)** Examples of Mitochondrion-to-Mitochondrion intrusion sites detected in **(D)** Set #1 and **(E)**
858 Set #2, displayed as partial (50nm) 2D averaged projections of raw EM and AIVE data (left panels),

859 rendered in 3D (centre panels), and with a colorimetric distance-map relative to other
860 mitochondria (right panels). For animations of these data, see Video 9. Additional examples are
861 provided in Fig.S5D-E. **(F)** 3D rendered examples of empty intrusion sites detected in each dataset.
862 Scalebars, 200nm; bounding dimensions of each 3D dataset, 1.5 x 1.5 x 1.5 µm.

863

864 Figure 8: Volume EM is essential for the analysis of mitochondrial intrusion sites

865 **(A)** 3D rendered examples of mitochondria containing intrusion sites, with their interior cavities
866 colourized by the category of intrusion. **(B)** Quantitative analysis comparing the membrane
867 volume mitochondria in the presence or absence of mitochondrial intrusions. **(C)** Bar chart
868 showing percentage of the mitochondrial population by their number of intrusions, with plot
869 markers indicating expected values calculated by a Poisson distribution of same average. **(D-F)**
870 Quantitative analyses of each intrusion cavity by category, showing their **(D)** total interior volume,
871 **(E)** radius of the largest inscribed sphere they could enclose, and **(F)** the length of their major
872 ellipsoidal axis. **(G)** Statistical modelling of Buffon's needle problem, showing the probability of
873 detecting an intact mitochondrial intrusion (solid line) or only half an intrusion (dashed line) when
874 an intrusion is present, as a function of the Z-depth ("d") in a hypothetical FIB-SEM dataset or TEM
875 section. Plot markers in B indicates value for individual mitochondria, in D-F indicates value for
876 individual intrusion cavities. Interquartile range for each chart indicated by box, median indicated
877 by horizontal lines, minimum and maximum indicated by whiskers. Scalebars; markers on scale
878 grid are 1000nm apart.

879

880

881 Figure S1: Supplementary AIVE descriptions and demonstrations.

882 **(A)** Signal matrix depicting how the input values for a voxel contribute to the output value during
883 AIVE (red line indicates approximate location of threshold used for 3D rendering and
884 segmentation). **(B)** 3D examples of other various categories of electron signal processed via AIVE,
885 as detected in the test dataset shown in Fig.1. **(C)** Quantification of the average ΔV per slice for
886 each 2-way comparison made between the model predictions from **Fig.1F** after the application of
887 a 10nm Gaussian blur (3D renders of corresponding data also provided in **Fig.S2B**). **(D)** 3D
888 renderings indicating the position of each static 3D probe used for mitochondrial distance

889 measurements in Fig.3, viewed from the front and above (membranes nearest to each 3D probe
890 are indicated by red shading). See Video 2 for rotation animation showing probe positions. **(E)**
891 Maximum value projection of AIVE processed data for the nucleus used in Fig.3, depicting the
892 position of each nuclear pore used for analysis in Fig.3N-T. **(F)** Averaged value projections of the
893 unprocessed EM data after spatial alignment for analyses shown in **Fig.3N-T**. Interquartile range
894 for chart indicated by box, median indicated by horizontal lines, minimum and maximum indicated
895 by whiskers. Scalebars; C, 1000nm; D, 100nm.

896

897 **Figure S2: Data at different stages of AIVE processing.**

898 **(A-C)** 3D depictions of 2D data shown in figures 1 & 2, showing the 3D surfaces generated using
899 **(A)** raw predictions, **(B)** blurred predictions, or **(C)** AIVE with one of six different trained models
900 (RF, J48, MLP, DT, JRip, and PART). **(D)** Raw distance measurements between the 3D probes
901 (shown in Fig.2H) and membrane surfaces under every condition shown in **A-C**. **(E-G)** raw AIVE
902 data from mitochondrion #33 (set 1) displayed as a sum projection from **(E)** the front and **(F)**
903 above (Also see Video 5), with **(G)** a orthoslice montage of EM and AIVE data through the
904 mitochondrial nanotunnel (position shown by box in F). Scalebars; 500nm.

905

906 **Figure S3: AIVE of mouse skeletal muscle.**

907 **(A-C)** AIVE reconstruction of mouse skeletal muscle tissue revealing mitochondrial nanotunnel
908 connections. **(A)** 3D rendering depicting myofibrils (red), mitochondria (purple) and sarcoplasmic
909 reticulum (gold) within a volume measuring 8 x 8 x 6.2 µm FIB-SEM volume, with **(B)** a rendered
910 cutaway displaying the interconnectivity of mitochondria within the tissue (mitochondrial
911 nanotunnels indicated by black arrow-heads). **(C)** Representative example of one nanotunnel
912 linking the mitochondrial network around a myofibril. See Video 6 for animated depiction of data
913 in A-C. Scalebar distances as indicated in figure.

914

915 **Figure S4: Simulated intrusive contacts.**

916 **(A-B)** 3D renderings of simulated contact between two spheres (128 voxel diameter) with
917 colorimetric distance scale indicating the distance of Sphere #1 from Sphere #2, **(A)** when both

structures are simple spheres, or **(B)** when Sphere #2 intrudes into Sphere #1. **(C-D)** Surface area histograms depicting the surface area percentage of Sphere #1 that is located within the indicated distances of Sphere #2, **(C)** when both structures are simple spheres, or **(D)** when Sphere #2 intrudes into Sphere #1 (Arrowhead in D indicates the anomalous peak discovered in Fig.6). **(E)** Illustrative description of "Buffon's Needle Problem" with corresponding equations, which describe the probability of a randomly distributed needle of known length ("L") overlapping a line, if those lines are regularly spaced by a known distance ("d"). Histogram data in C-D are surface area percentages binned into 5 voxel distance brackets relative to Sphere #2. Scalebars in A-B, 10 voxels.

Figure S5: Additional examples of intrusive contact sites.

(A-C) Additional examples of ER-to-Mitochondrion intrusion sites, displayed as partial (50nm) 2D averaged projections of raw EM and AIVE data (left panels), rendered in 3D (centre panels), and with a colorimetric distance-map relative to the ER (right panels). **(D-E)** Additional examples of Mitochondrion-to-Mitochondrion intrusion sites, displayed as partial (50nm) 2D averaged projections of raw EM and AIVE data (left panels), rendered in 3D (centre panels), and with a colorimetric distance-map relative to other mitochondria (right panels). Scalebars, 200nm; bounding dimensions of each 3D dataset, 1.5 x 1.5 x 1.5 µm.

938 # Video Legends:

939 ## Video 1: General membrane distance probes

940 Animated rotation of the test volume, depicting the 3D membrane probe positions (from Fig.2H)
941 used for membrane distance measurements in Fig.2-3. General membranes are shown in diffuse
942 navy blue, while membranes nearest to a 3D probe are indicated by red shading.

943 ## Video 2: Mitochondrial membrane distance probes

944 Animated rotation of the test volume, depicting the 3D mitochondrial membrane probe positions
945 (from Fig.S1D) used for mitochondrial membrane distance measurements in Fig.4. Mitochondrial
946 membranes are shown in diffuse navy blue, while membranes nearest to a 3D probe are indicated
947 by red shading.

948 ## Video 3: Overview cutaways

949 Animated cutaways of the data presented in Fig.4B-D. The video begins with all organelles shown,
950 before cutting away the endoplasmic reticulum (ER) and nuclear envelope (Nu), followed by the
951 Golgi and vesicles (VE), and finally, the early endosomes (EE), late endosomes (LE), and lipid
952 droplets (LD). The video concludes by revealing these organelles in reverse order. Render key is
953 provided within the animation.

954 ## Video 4: Smallest and largest mitochondria

955 Animation depicting the structure of the smallest (Fig.5A) and largest (Fig.5B) volumed
956 mitochondria from figure 5. Render key is provided within the animation.

957 ## Video 5: Spherical, nanotunneling, and unremarkable mitochondria

958 Animation depicting the structure of the most spherical mitochondrion (Fig.5F), a nanotunneling
959 mitochondrion (Fig.5C), and the “least remarkable” mitochondrion (Fig.5G) from figure 5. Render
960 key is provided within the animation.

961 ## Video 6: AIVE of mouse skeletal muscle

962 Animation of rendered data shown in Fig.S5, displaying an AIVE reconstruction of FIB-SEM data
963 from mouse skeletal muscle tissue, measuring 8 x 8 x 6.2 µm. As the video begins, myofibrils (red)
964 and sarcoplasmic reticulum (gold) are cut away to reveal the mitochondrial network (purple).
965 Black arrowheads then appear to highlight the mitochondrial nanotunnels, as the camera pans

around the dataset. The video concludes by focussing on a specific mitochondrial nanotunnel which is tightly wrapped around a myofibril, thus connecting mitochondria on opposing sides of the myofibril.

Video 7: Most elongated and longest mitochondria

Animation depicting the structure of the most elongated (Fig.5D) and longest (Fig.5E) mitochondria from figure 5. Render key is provided within the animation.

Video 8: Intrusive contact by ER

Animation of the ER intrusions (Fig.7A-C) depicted in figure 7. The video begins with the full ROI centred around the intrusion sites, with colourations indicated by render key. As the intruding ER fades away, the mitochondrial surface is transitioned to the distance-map (0 to 100nm) colour scale shown in figure 7, before rotation of the camera vertically over the datasets. The video concludes by returning to the initial shading.

Video 9: Intrusive contact by mitochondria

Animation of the mitochondrial intrusions (Fig.7D-E) depicted in figure 7. The video begins with the full ROI centred around the intrusion sites, with colourations indicated by render key. As the intruding mitochondrion fades away, the mitochondrial surfaces are transitioned to the distance-map (0 to 100nm) colour scale shown in figure 7, before rotation of the camera vertically over the datasets. The video concludes by returning to the initial shading.

References

1. Voeltz, G.K., et al., *Making the connection: How membrane contact sites have changed our view of organelle biology.* Cell, 2024. **187**(2): p. 257-270.
2. Scorrano, L., et al., *Coming together to define membrane contact sites.* Nature Communications, 2019. **10**(1).
3. Flis, V.V. and G. Daum, *Lipid Transport between the Endoplasmic Reticulum and Mitochondria.* Cold Spring Harbor Perspectives in Biology, 2013. **5**(6): p. a013235-a013235.
4. Schrader, M., et al., *The different facets of organelle interplay—an overview of organelle interactions.* Frontiers in Cell and Developmental Biology, 2015. **3**.
5. Shai, N., M. Schuldiner, and E. Zalckvar, *No peroxisome is an island - Peroxisome contact sites.* Biochim Biophys Acta, 2016. **1863**(5): p. 1061-9.
6. Coleman, R.A., *It takes a village: channeling fatty acid metabolism and triacylglycerol formation via protein interactomes.* J Lipid Res, 2019. **60**(3): p. 490-497.
7. Wang, Y., et al., *Nanoparticle-Driven Controllable Mitochondrial Regulation through Lysosome-Mitochondria Interactome.* ACS Nano, 2022. **16**(8): p. 12553-12568.
8. Venditti, R., M.C. Masone, and M.A. De Matteis, *ER-Golgi membrane contact sites.* Biochem Soc Trans, 2020. **48**(1): p. 187-197.
9. Valm, A.M., et al., *Applying systems-level spectral imaging and analysis to reveal the organelle interactome.* Nature, 2017. **546**(7656): p. 162-167.
10. Jing, J., et al., *A molecular toolbox for interrogation of membrane contact sites.* The Journal of Physiology, 2019. **598**(9): p. 1725-1739.
11. Huang, X., et al., *Current and Emerging Approaches for Studying Inter-Organelle Membrane Contact Sites.* Frontiers in Cell and Developmental Biology, 2020. **8**.
12. Peng, L., et al., *The Advances and Challenges of Deep Learning Application in Biological Big Data Processing.* Current Bioinformatics, 2018. **13**(4): p. 352-359.
13. Xu, C.S., et al., *Transforming FIB-SEM Systems for Large-Volume and*, in *Volume Microscopy*. 2020. p. 221-243.
14. Gallusser, B., et al., *Deep neural network automated segmentation of cellular structures in volume electron microscopy.* Journal of Cell Biology, 2023. **222**(2).
15. Liu, L., et al., *DeepContact: High-throughput quantification of membrane contact sites based on electron microscopy imaging.* Journal of Cell Biology, 2022. **221**(9).
16. Nguyen, T.N., et al., *ATG4 family proteins drive phagophore growth independently of the LC3/GABARAP lipidation system.* Mol Cell, 2021. **81**(9): p. 2013-2030 e9.
17. Richard, M.D. and R.P. Lippmann, *Neural Network Classifiers Estimate Bayesian a posteriori Probabilities.* Neural Computation, 1991. **3**(4): p. 461-483.
18. Rumelhart, D.E., G.E. Hinton, and R.J. Williams, *Learning representations by back-propagating errors.* Nature, 1986. **323**(6088): p. 533-536.
19. Wang, Z., E. Wang, and Y. Zhu, *Image segmentation evaluation: a survey of methods.* Artificial Intelligence Review, 2020. **53**(8): p. 5637-5674.
20. Lee, R.G., et al., *Quantitative subcellular reconstruction reveals a lipid mediated inter-organelle biogenesis network.* Nat Cell Biol, 2024. **26**(1): p. 57-71.
21. Gibson, S.F.F., *Constrained elastic surface nets: Generating smooth surfaces from binary segmented data*, in *Medical Image Computing and Computer-Assisted Intervention — MICCAI'98*. 1998. p. 888-898.
22. Lorensen, W.E. and H.E. Cline, *Marching cubes: A high resolution 3D surface construction algorithm.* ACM SIGGRAPH Computer Graphics, 1987. **21**(4): p. 163-169.
23. Kim, S., et al., *A novel interpolation scheme for dual marching cubes on octree volume fraction data.* Computers & Graphics, 2017. **66**: p. 169-178.
24. Thevathasan, J.V., et al., *Nuclear pores as versatile reference standards for quantitative superresolution microscopy.* Nature Methods, 2019. **16**(10): p. 1045-1053.

1038 25. Schuller, A.P., et al., *The cellular environment shapes the nuclear pore complex architecture.* Nature,
1039 2021. **598**(7882): p. 667-671.
1040 26. Zimmerli, C.E., et al., *Nuclear pores dilate and constrict in cellulo.* Science, 2021. **374**(6573).
1041 27. Drozdz, M.M., et al., *Formation of a nucleoplasmic reticulum requires de novo assembly of nascent*
1042 *phospholipids and shows preferential incorporation of nascent lamins.* Scientific Reports, 2017. **7**(1).
1043 28. Vincent, A.E., et al., *Mitochondrial Nanotunnels.* Trends Cell Biol, 2017. **27**(11): p. 787-799.
1044 29. Friedman, J.R., et al., *ER sliding dynamics and ER–mitochondrial contacts occur on acetylated*
1045 *microtubules.* Journal of Cell Biology, 2010. **190**(3): p. 363-375.
1046 30. Robertson, J.M. and A.F. Siegel, *Designing Buffon's Needle for a Given Crossing Distribution.* The
1047 American Mathematical Monthly, 2018. **93**(2): p. 116-119.
1048 31. Lebovitz, S., N. Levina, and H. Lifshitz-Assa, *Is AI Ground Truth Really True? The Dangers of Training*
1049 *and Evaluating AI Tools Based on Experts' Know-What.* MIS Quarterly, 2021. **45**(3): p. 1501-1526.
1050 32. Woodhouse, I.H., *On 'ground' truth and why we should abandon the term.* Journal of Applied
1051 Remote Sensing, 2021. **15**(04).
1052 33. Zick, M., R. Rabl, and A.S. Reichert, *Cristae formation-linking ultrastructure and function of*
1053 *mitochondria.* Biochim Biophys Acta, 2009. **1793**(1): p. 5-19.
1054 34. Linda, S., et al., *Mitochondrial Diseases and Myopathies: A Series of Muscle Biopsy Specimens with*
1055 *Ultrastructural Changes in the Mitochondria.* Ultrastructural Pathology, 2009. **16**(3): p. 263-275.
1056 35. Vincent, A.E., et al., *The Spectrum of Mitochondrial Ultrastructural Defects in Mitochondrial*
1057 *Myopathy.* Scientific Reports, 2016. **6**(1).
1058 36. Jenkins, B.C., et al., *Mitochondria in disease: changes in shapes and dynamics.* Trends Biochem Sci,
1059 2024. **49**(4): p. 346-360.
1060 37. Siegmund, S.E., et al., *Three-Dimensional Analysis of Mitochondrial Crista Ultrastructure in a Patient*
1061 *with Leigh Syndrome by In Situ Cryoelectron Tomography.* iScience, 2018. **6**: p. 83-91.
1062 38. Ryu, K.W., et al., *Cellular ATP demand creates metabolically distinct subpopulations of*
1063 *mitochondria.* Nature, 2024.
1064 39. Huang, X., et al., *Kissing and nanotunneling mediate intermitochondrial communication in the*
1065 *heart.* Proc Natl Acad Sci U S A, 2013. **110**(8): p. 2846-51.
1066 40. Lavorato, M., et al., *Increased mitochondrial nanotunneling activity, induced by calcium imbalance,*
1067 *affects intermitochondrial matrix exchanges.* Proc Natl Acad Sci U S A, 2017. **114**(5): p. E849-E858.
1068 41. Miyazono, Y., et al., *Uncoupled mitochondria quickly shorten along their long axis to form indented*
1069 *spheroids, instead of rings, in a fission-independent manner.* Scientific Reports, 2018. **8**(1).
1070 42. Giacomello, M., et al., *The cell biology of mitochondrial membrane dynamics.* Nature Reviews
1071 Molecular Cell Biology, 2020. **21**(4): p. 204-224.
1072 43. Lackner, L.L., *The Expanding and Unexpected Functions of Mitochondria Contact Sites.* Trends in Cell
1073 Biology, 2019. **29**(7): p. 580-590.
1074 44. Hertz, H., *Ueber die Berührung fester elastischer Körper.* Journal für die reine und angewandte
1075 Mathematik, 1882. **1882**(92): p. 156-171.
1076 45. Scorrano, L., et al., *Coming together to define membrane contact sites.* Nat Commun, 2019. **10**(1):
1077 p. 1287.
1078 46. Yeo, H.K., et al., *Phospholipid transfer function of PTPIP51 at mitochondria-associated ER*
1079 *membranes.* EMBO Rep, 2021. **22**(6): p. e51323.
1080 47. Freyre, C.A.C., et al., *MIGA2 Links Mitochondria, the ER, and Lipid Droplets and Promotes De Novo*
1081 *Lipogenesis in Adipocytes.* Mol Cell, 2019. **76**(5): p. 811-825 e14.
1082 48. Kim, H., et al., *Structural basis for mitoguardin-2 mediated lipid transport at ER-mitochondrial*
1083 *membrane contact sites.* Nat Commun, 2022. **13**(1): p. 3702.
1084 49. Naon, D., et al., *Splice variants of mitofusin 2 shape the endoplasmic reticulum and tether it to*
1085 *mitochondria.* Science, 2023. **380**(6651): p. eadh9351.
1086 50. De Vos, K.J., et al., *VAPB interacts with the mitochondrial protein PTPIP51 to regulate calcium*
1087 *homeostasis.* Hum Mol Genet, 2012. **21**(6): p. 1299-311.
1088 51. Stoica, R., et al., *ER-mitochondria associations are regulated by the VAPB-PTPIP51 interaction and*
1089 *are disrupted by ALS/FTD-associated TDP-43.* Nat Commun, 2014. **5**: p. 3996.

1090 52. Csordas, G., et al., *Imaging interorganelle contacts and local calcium dynamics at the ER-*
1091 *mitochondrial interface.* Mol Cell, 2010. **39**(1): p. 121-32.
1092 53. Seligman, A.M., H.L. Wasserkrug, and J.S. Hanker, *A new staining method (OTO) for enhancing*
1093 *contrast of lipid--containing membranes and droplets in osmium tetroxide--fixed tissue with*
1094 *osmiophilic thiocarbohydrazide(TCH).* J Cell Biol, 1966. **30**(2): p. 424-32.
1095 54. Silva, M.T., F.C. Guerra, and M.M. Magalhaes, *The fixative action of uranyl acetate in electron*
1096 *microscopy.* Experientia, 1968. **24**(10): p. 1074.
1097 55. Walton, J., *Lead aspartate, an en bloc contrast stain particularly useful for ultrastructural*
1098 *enzymology.* J Histochem Cytochem, 1979. **27**(10): p. 1337-42.
1099 56. Arganda-Carreras, I., et al., *Consistent and Elastic Registration of Histological Sections Using Vector-*
1100 *Spline Regularization*, in *Computer Vision Approaches to Medical Image Analysis*. 2006. p. 85-95.
1101 57. Rueden, C.T., et al., *ImageJ2: ImageJ for the next generation of scientific image data.* BMC
1102 Bioinformatics, 2017. **18**(1).
1103 58. Frank, E., et al., *Data mining in bioinformatics using Weka.* Bioinformatics, 2004. **20**(15): p. 2479-
1104 2481.
1105 59. Arganda-Carreras, I., et al., *Trainable Weka Segmentation: a machine learning tool for microscopy*
1106 *pixel classification.* Bioinformatics, 2017. **33**(15): p. 2424-2426.
1107 60. Schindelin, J., et al., *Fiji: an open-source platform for biological-image analysis.* Nat Methods, 2012.
1108 **9**(7): p. 676-82.
1109 61. Huang, B., et al., *Deep Convolutional Segmentation of Remote Sensing Imagery: A Simple and*
1110 *Efficient Alternative to Stitching Output Labels*, in *IGARSS 2018 - 2018 IEEE International Geoscience*
1111 *and Remote Sensing Symposium*. 2018. p. 6899-6902.
1112 62. Fernandez, R. and C. Moisy, *Fijiyama: a registration tool for 3D multimodal time-lapse imaging.*
1113 Bioinformatics, 2021. **37**(10): p. 1482-1484.
1114 63. Legland, D., I. Arganda-Carreras, and P. Andrey, *MorphoLibJ: integrated library and plugins for*
1115 *mathematical morphology with ImageJ.* Bioinformatics, 2016. **32**(22): p. 3532-3534.

1116

Figure 1

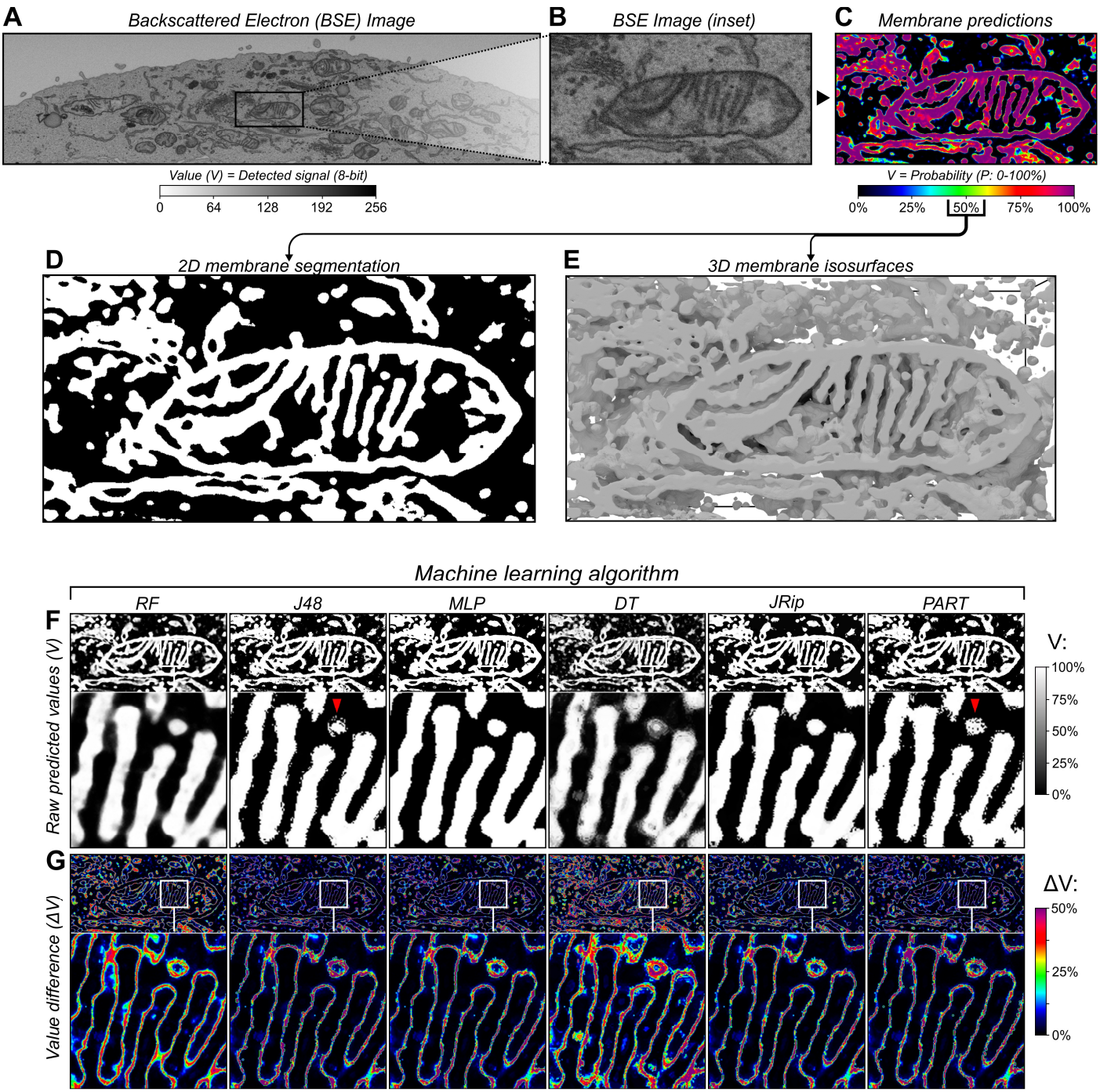
A
Backscattered Electron (BSE) Image
B
BSE Image (inset)
C
Membrane predictions
Value (V) = Detected signal (8-bit)
0
64
128
192
256
V = Probability (P: 0-100%)
0%
25%
50%
75%
100%
D
2D membrane segmentation
E
3D membrane isosurfaces
Machine learning algorithm
RF
J48
MLP
DT
JRip
PART
F
Raw predicted values (V)
V:
100%
75%
50%
25%
0%
G
Value difference (ΔV)
ΔV:
50%
25%
0%

Figure 2

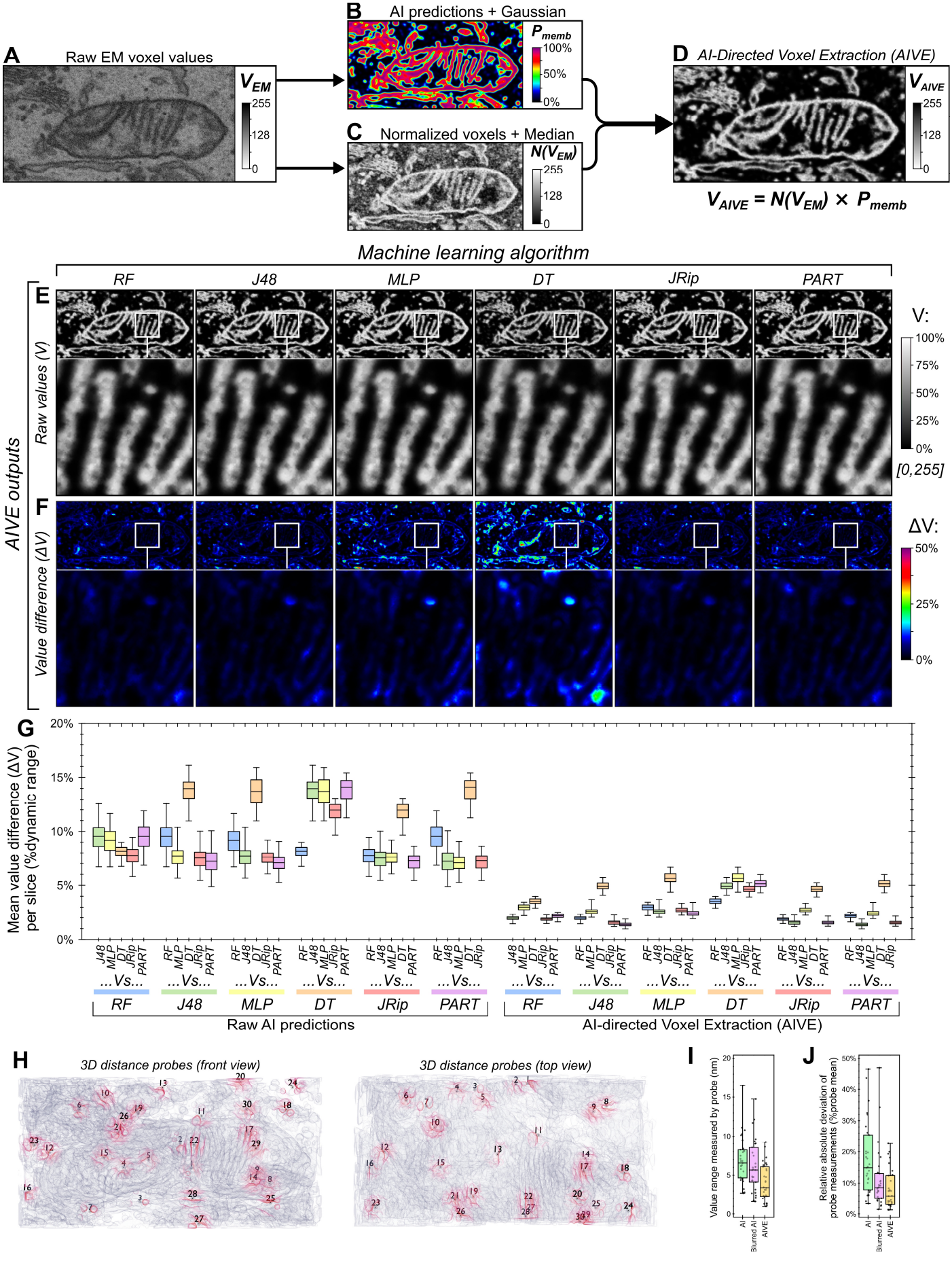
A
Raw EM voxel values
V_{EM}
255
128
0
B
AI predictions + Gaussian
P_{memb}
100%
50%
0%
C
Normalized voxels + Median
$N(V_{EM})$
255
128
0
D
AI-Directed Voxel Extraction (AIVE)
V_{AIVE}
255
128
0
$V_{AIVE} = N(V_{EM}) \times P_{memb}$
Machine learning algorithm
RF
J48
MLP
DT
JRip
PART
AIVE outputs
E
Raw values (V)
V:
100%
75%
50%
25%
0%
[0,255]
F
Value difference (ΔV)
ΔV:
50%
25%
0%
G
Mean value difference (ΔV) per slice (%dynamic range)
20%
15%
10%
5%
0%
...Vs...
Raw AI predictions
AI-directed Voxel Extraction (AIVE)
H
3D distance probes (front view)
3D distance probes (top view)
I
Value range measured by probe (nm)
AI
Blurred AI
AIVE
J
Relative absolute deviation of probe measurements (%probe mean)
50%
40%
30%
20%
10%
0%

Figure 3

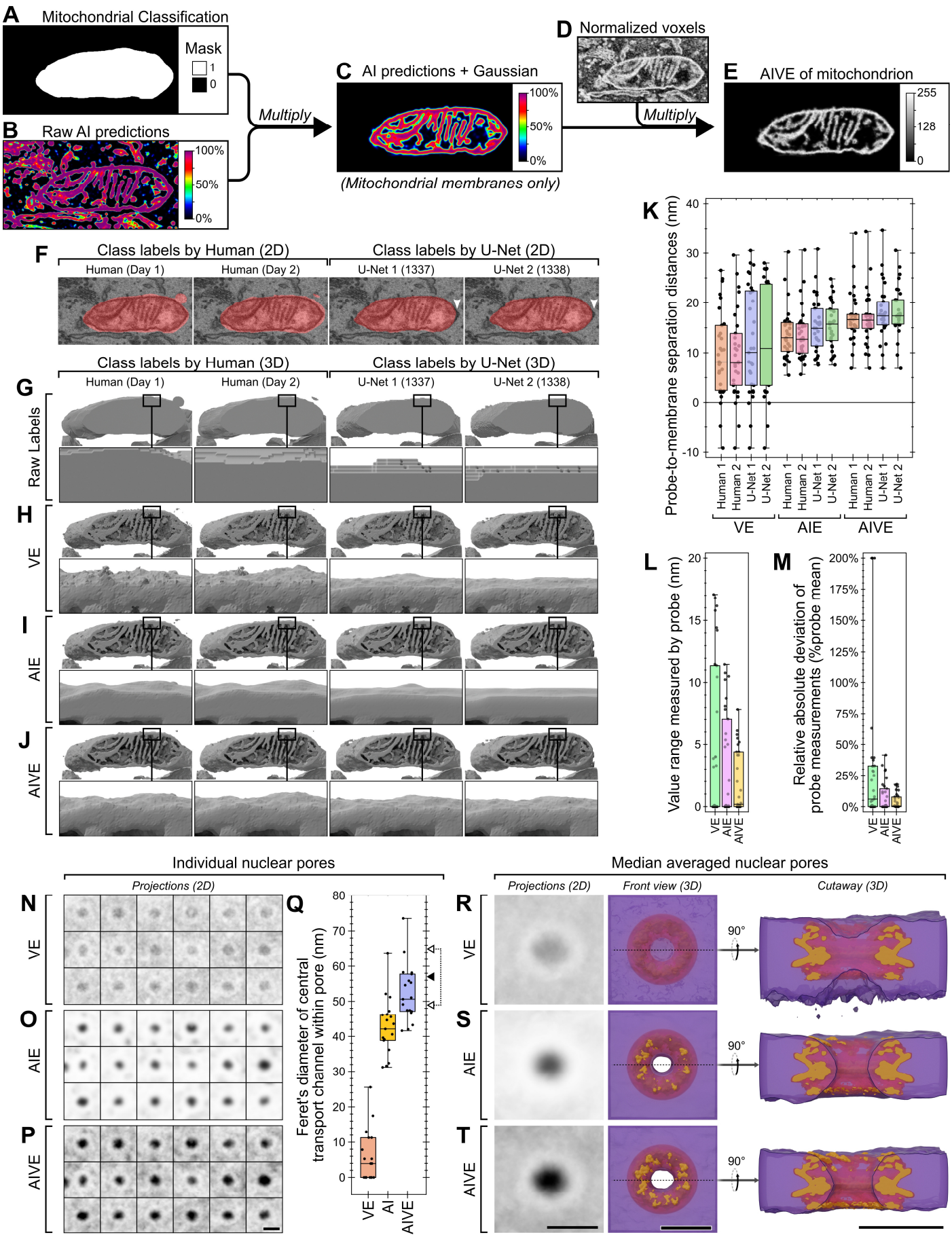
A Mitochondrial Classification
Mask
1
0
B Raw AI predictions
100%
50%
0%
Multiply
C AI predictions + Gaussian
100%
50%
0%
(Mitochondrial membranes only)
D Normalized voxels
Multiply
E AIVE of mitochondrion
255
128
0
F
Class labels by Human (2D)
Class labels by U-Net (2D)
Human (Day 1)
Human (Day 2)
U-Net 1 (1337)
U-Net 2 (1338)
G
Class labels by Human (3D)
Class labels by U-Net (3D)
Raw Labels
H
VE
I
AIE
J
AIVE
K
Probe-to-membrane separation distances (nm)
Human 1
Human 2
U-Net 1
U-Net 2
VE
AIE
AIVE
L
Value range measured by probe (nm)
M
Relative absolute deviation of probe measurements (%probe mean)
Individual nuclear pores
Projections (2D)
N
VE
O
AIE
P
AIVE
Q
Feret's diameter of central transport channel within pore (nm)
VE
AI
AIVE
Median averaged nuclear pores
Projections (2D)
Front view (3D)
Cutaway (3D)
R
VE
S
AIE
T
AIVE
90°

Figure 4

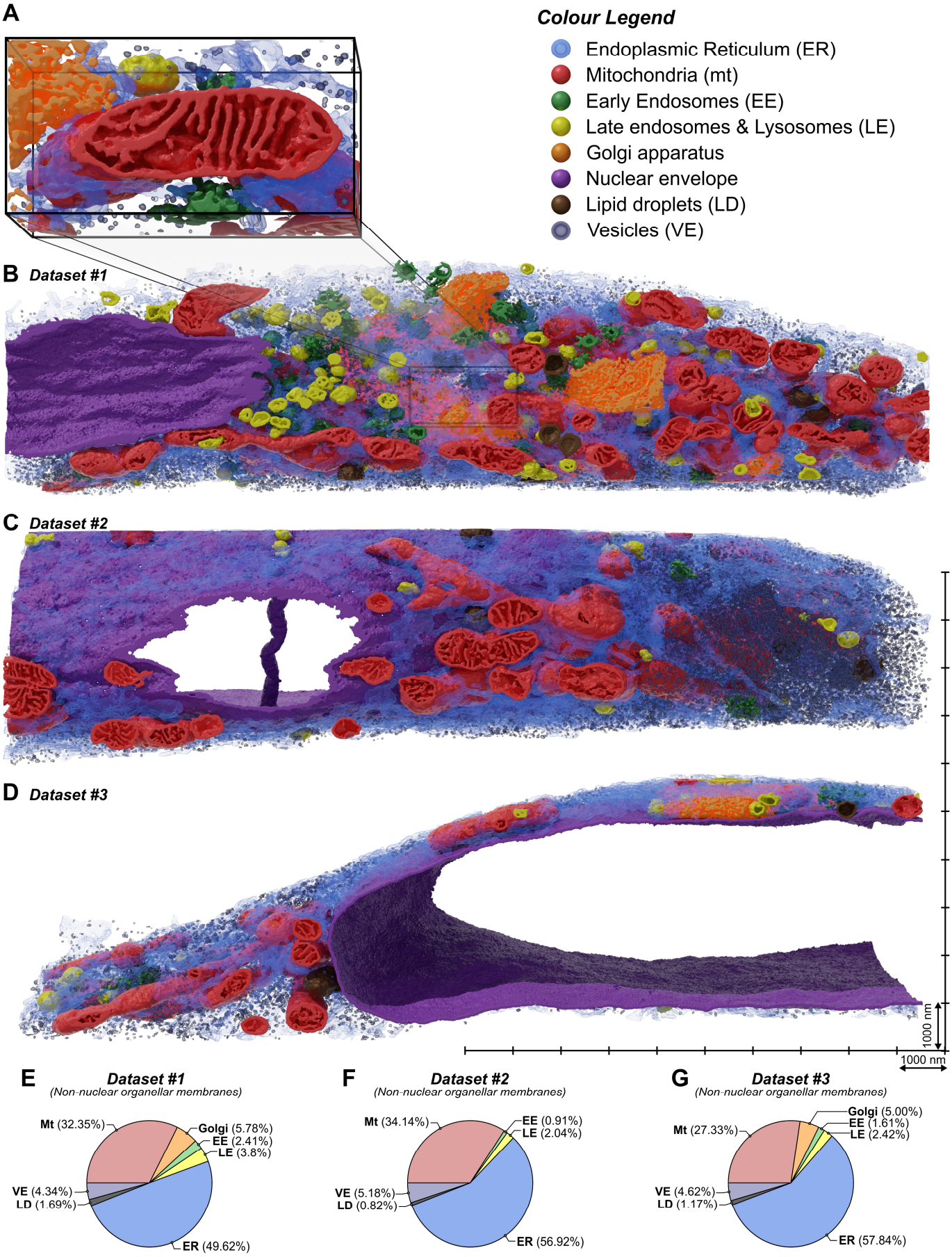
A
Colour Legend
Endoplasmic Reticulum (ER)
Mitochondria (mt)
Early Endosomes (EE)
Late endosomes & Lysosomes (LE)
Golgi apparatus
Nuclear envelope
Lipid droplets (LD)
Vesicles (VE)
B Dataset #1
C Dataset #2
D Dataset #3
1000 nm
1000 nm
E Dataset #1
(Non-nuclear organellar membranes)
Mt (32.35%)
Golgi (5.78%)
EE (2.41%)
LE (3.8%)
VE (4.34%)
LD (1.69%)
ER (49.62%)
F Dataset #2
(Non-nuclear organellar membranes)
Mt (34.14%)
EE (0.91%)
LE (2.04%)
VE (5.18%)
LD (0.82%)
ER (56.92%)
G Dataset #3
(Non-nuclear organellar membranes)
Golgi (5.00%)
EE (1.61%)
LE (2.42%)
Mt (27.33%)
VE (4.62%)
LD (1.17%)
ER (57.84%)

Figure 5

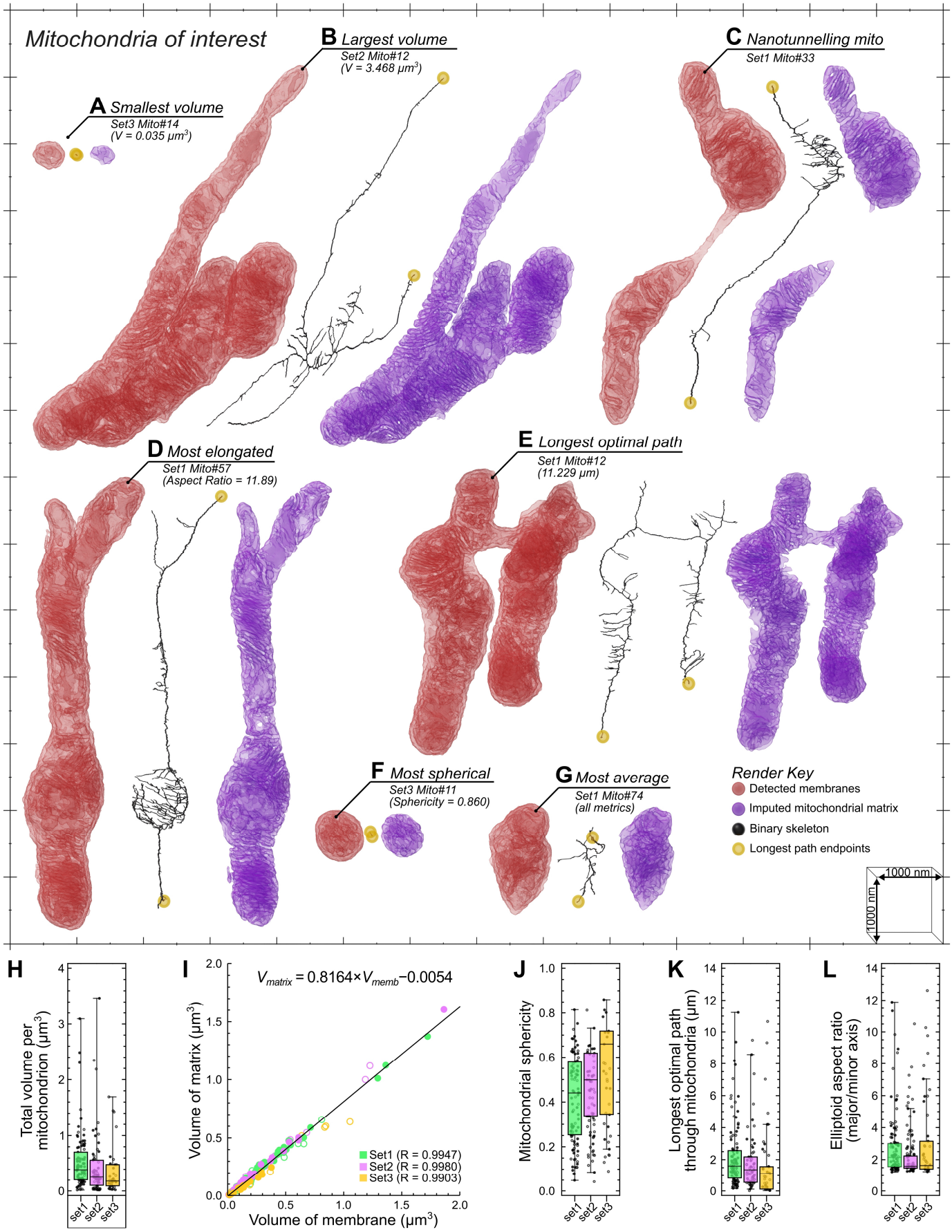
Mitochondria of interest
A Smallest volume
Set3 Mito#14
(V = 0.035 μm³)
B Largest volume
Set2 Mito#12
(V = 3.468 μm³)
C Nanotunnelling mito
Set1 Mito#33
D Most elongated
Set1 Mito#57
(Aspect Ratio = 11.89)
E Longest optimal path
Set1 Mito#12
(11.229 μm)
F Most spherical
Set3 Mito#11
(Sphericity = 0.860)
G Most average
Set1 Mito#74
(all metrics)
Render Key
Detected membranes
Imputed mitochondrial matrix
Binary skeleton
Longest path endpoints
1000 nm
1000 nm

H
Total volume per mitochondrion (μm³)
set1
set2
set3
I
$V_{matrix} = 0.8164 \times V_{memb} - 0.0054$
Volume of matrix (μm³)
Volume of membrane (μm³)
Set1 (R = 0.9947)
Set2 (R = 0.9980)
Set3 (R = 0.9903)
J
Mitochondrial sphericity
K
Longest optimal path through mitochondria (μm)
L
Ellipsoid aspect ratio (major/minor axis)

Figure 6

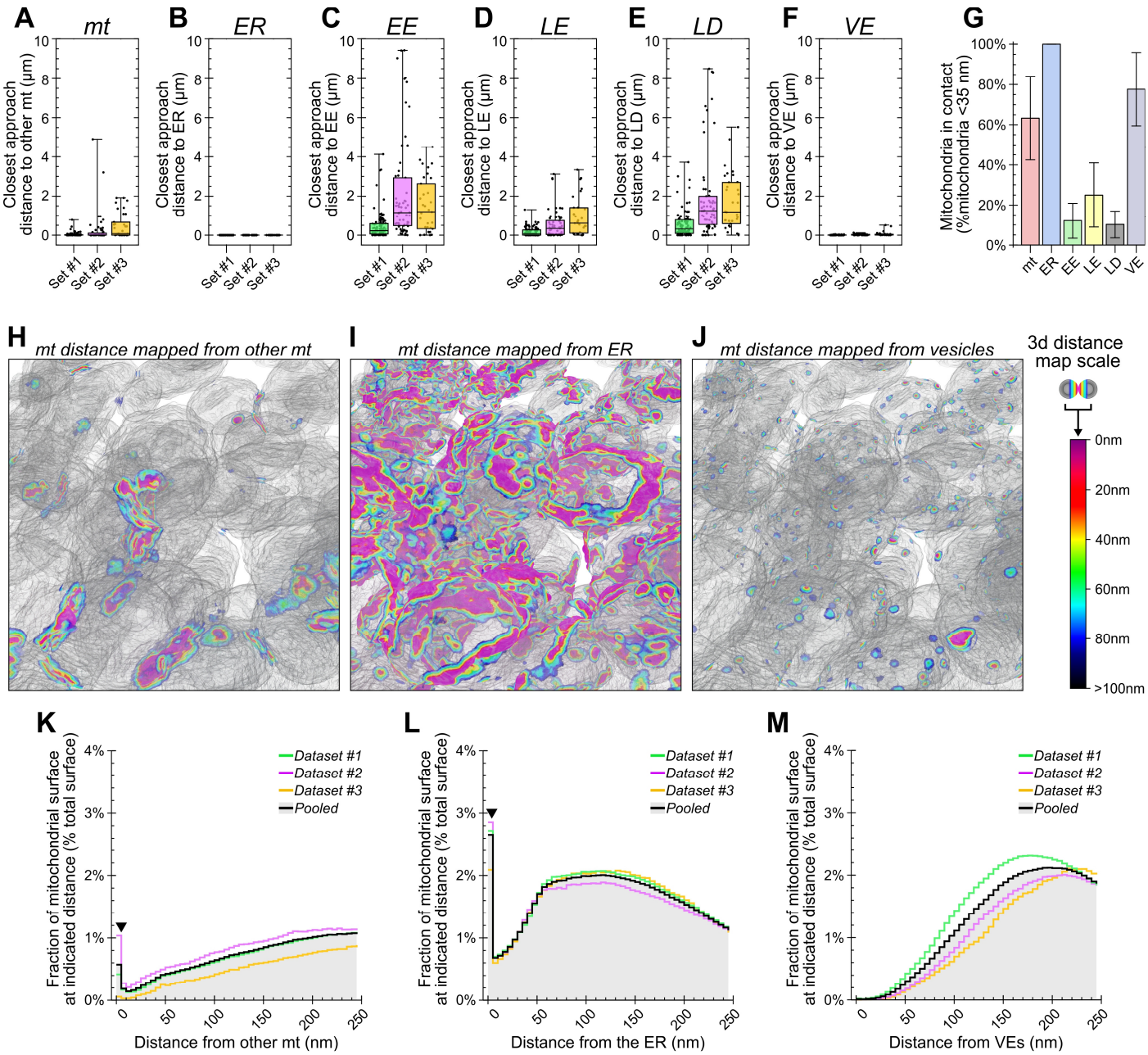
A
mt
Closest approach distance to other mt (µm)
B
ER
Closest approach distance to ER (µm)
C
EE
Closest approach distance to EE (µm)
D
LE
Closest approach distance to LE (µm)
E
LD
Closest approach distance to LD (µm)
F
VE
Closest approach distance to VE (µm)
Set #1
Set #2
Set #3
G
Mitochondria in contact (%mitochondria <35 nm)
mt
ER
EE
LE
LD
VE
H
mt distance mapped from other mt
I
mt distance mapped from ER
J
mt distance mapped from vesicles
3d distance map scale
0nm
20nm
40nm
60nm
80nm
>100nm
K
Fraction of mitochondrial surface at indicated distance (% total surface)
Dataset #1
Dataset #2
Dataset #3
Pooled
Distance from other mt (nm)
L
Distance from the ER (nm)
M
Distance from VEs (nm)

Figure 7

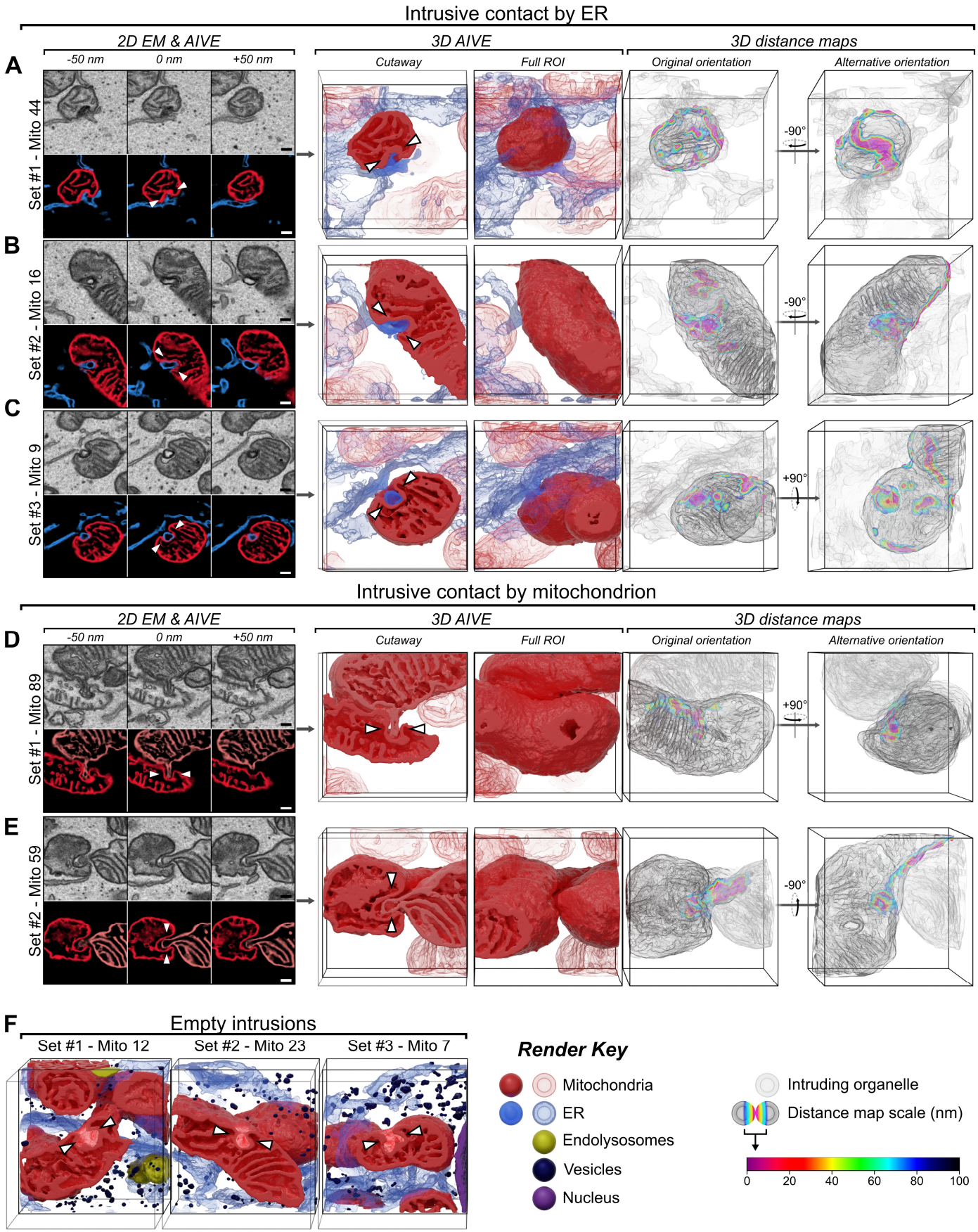
Intrusive contact by ER
2D EM & AIVE
3D AIVE
3D distance maps
-50 nm
0 nm
+50 nm
Cutaway
Full ROI
Original orientation
Alternative orientation
A
Set #1 - Mito 44
B
Set #2 - Mito 16
C
Set #3 - Mito 9
-90°
+90°
Intrusive contact by mitochondrion
D
Set #1 - Mito 89
E
Set #2 - Mito 59
F
Empty intrusions
Set #1 - Mito 12
Set #2 - Mito 23
Set #3 - Mito 7
Render Key
Mitochondria
ER
Endolysosomes
Vesicles
Nucleus
Intruding organelle
Distance map scale (nm)
0
20
40
60
80
100

Figure 8

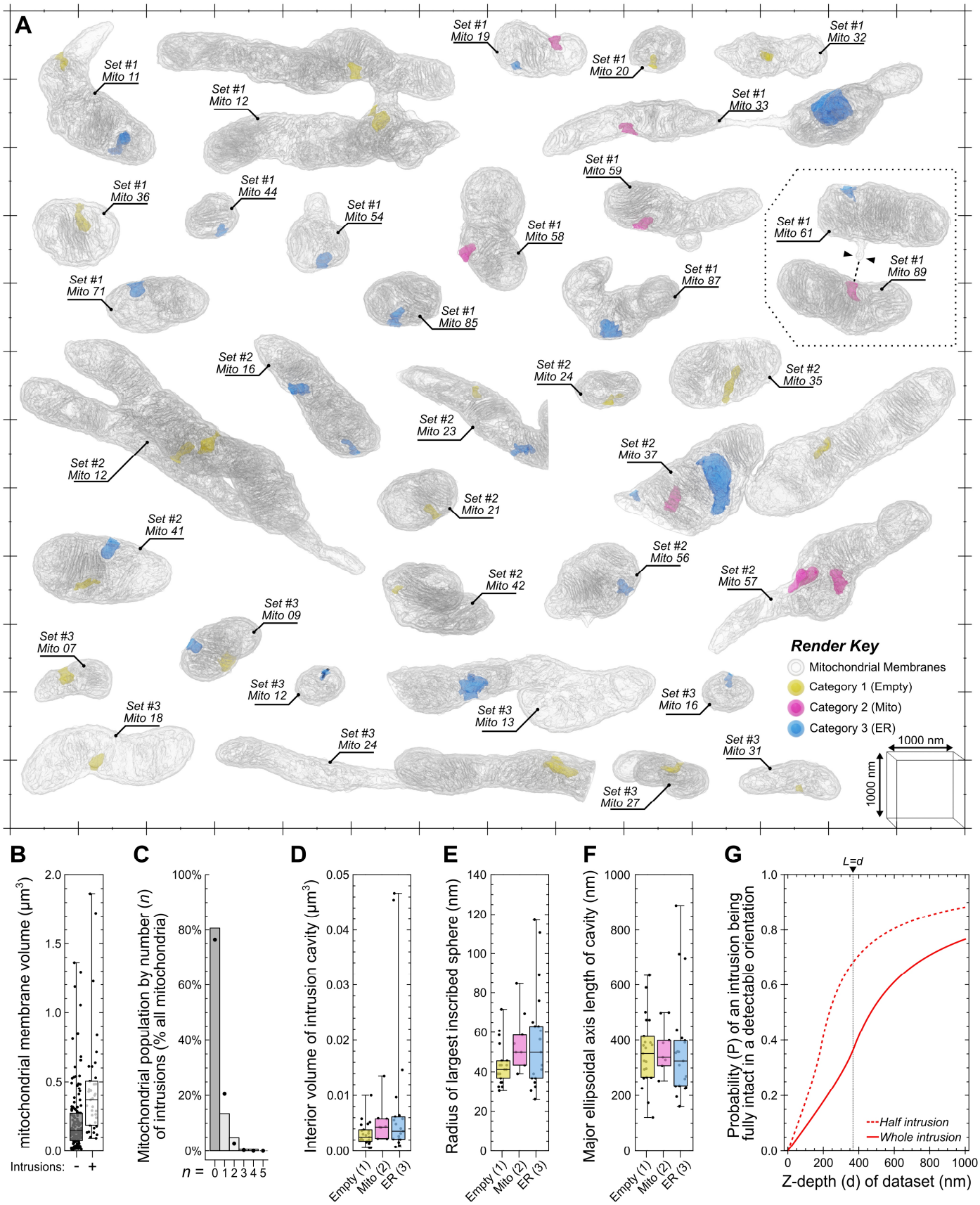
A
Set #1 Mito 11
Set #1 Mito 12
Set #1 Mito 19
Set #1 Mito 20
Set #1 Mito 32
Set #1 Mito 33
Set #1 Mito 36
Set #1 Mito 44
Set #1 Mito 54
Set #1 Mito 58
Set #1 Mito 59
Set #1 Mito 61
Set #1 Mito 89
Set #1 Mito 71
Set #1 Mito 85
Set #1 Mito 87
Set #2 Mito 16
Set #2 Mito 24
Set #2 Mito 35
Set #2 Mito 23
Set #2 Mito 12
Set #2 Mito 37
Set #2 Mito 21
Set #2 Mito 41
Set #2 Mito 56
Set #2 Mito 42
Set #2 Mito 57
Set #3 Mito 09
Set #3 Mito 07
Set #3 Mito 12
Set #3 Mito 16
Set #3 Mito 18
Set #3 Mito 13
Set #3 Mito 24
Set #3 Mito 31
Set #3 Mito 27
Render Key
Mitochondrial Membranes
Category 1 (Empty)
Category 2 (Mito)
Category 3 (ER)
1000 nm
1000 nm
B
mitochondrial membrane volume (µm³)
Intrusions: - +
C
Mitochondrial population by number (n) of intrusions (% all mitochondria)
n = 0 1 2 3 4 5
D
Interior volume of intrusion cavity (µm³)
Empty (1)
Mito (2)
ER (3)
E
Radius of largest inscribed sphere (nm)
Empty (1)
Mito (2)
ER (3)
F
Major ellipsoidal axis length of cavity (nm)
Empty (1)
Mito (2)
ER (3)
G
L=d
Probability (P) of an intrusion being fully intact in a detectable orientation
Half intrusion
Whole intrusion
Z-depth (d) of dataset (nm)